Formation and coarsening of the concertina magnetization pattern in elongated thin-film elements

Jutta Steiner
Centre de Mathémathiques Appliqueées, École Polytechnique, 91128 Palaiseau Cedex, France

Rudolf Schäfer and Holm Wieczoreck
Leibniz Institute for Solid State and Materials Research Dresden (IFW Dresden), Institute for Metallic Materials, Helmholtzstraße 20, 01069 Dresden, Germany

Jeffrey McCord
Institute for Materials Science, Technical Faculty of CAU Kiel, Kaiserstraße 2, 24143 Kiel, Germany

Felix Otto
Max Planck Institute for Mathematics in the Sciences, Inselstraße 22, 04103 Leipzig, Germany
(Received 5 July 2011; revised manuscript received 23 November 2011; published 12 March 2012)

The concertina is a magnetization pattern in elongated thin-film elements of a soft ferromagnetic material. It is a ubiquitous domain pattern that occurs in the process of magnetization reversal in the direction of the long axis of the small element. Van den Berg and Vatvani [IEEE Trans. Magn. **18**, 880 (1982)] argued that this pattern grows out of the flux-closure domains at the sample's tips as the external field is reduced. Based on experimental observations and theory, we argue that in sufficiently elongated thin-film elements the concertina pattern rather bifurcates from an oscillatory buckling mode. Typical sample widths and thicknesses are of the order of 10-100 μm and of the order of 10-150 nm, respectively. Using a reduced model that is derived by asymptotic analysis from the micromagnetic energy and that is also investigated by means of numerical simulation, we quantitatively predict the average period of the concertina pattern and qualitatively predict its hysteresis. In particular, we argue that the experimentally observed coarsening of the concertina pattern is due to secondary bifurcations related to an Eckhaus instability. We also link the concertina pattern to the magnetization ripple and discuss the effect of a weak (crystalline or induced) anisotropy.

DOI: 10.1103/PhysRevB.85.104407 PACS number(s): 75.70.Kw, 75.60.Jk, 75.60.Ch

I. INTRODUCTION

To our knowledge, the term *concertina* was introduced by van den Berg and Vatvani in Ref. 1, p. 880. In that paper the authors explain the formation of this domain pattern in Permalloy thin-film elements that are fairly thick (thickness $t = 350$ nm), with a rectangular cross section (width $\ell = 15$ μm) that is *not too elongated* (length 60 μm). After near saturation along the long axis, a concertina pattern grows out of the flux-closure domains at the short edges of the cross section during subsequent reduction of the external field $\mathbf{H}_{\text{ext}}$, until the pattern eventually invades the entire sample; see right image in Fig. 1. Our experimental observations suggest that in *very elongated* samples (length 2000 μm, thickness 10 to 150 nm, width 10 to 100 μm) a bifurcation is at the origin of the concertina. As a consequence, the pattern forms simultaneously all over the sample; see Fig. 2.

The organization of our paper is as follows: After introducing the micromagnetic energy in Sec. I A we report on van den Berg's explanation and further previous related work in more detail in Sec. I B. We go on with a comparison of our results to van den Berg's predictions in Sec. I C. Section I D contains a description of the experimental setup and details on the samples that we investigate. Our analysis, that is based on the micromagnetic energy, starts with a linear stability analysis of the uniform magnetization under field reversal (nucleation) in Secs. I E and I F. A bifurcation analysis is performed in Sec. I I based on a reduced model derived from the micromagnetic model in Sec. I H. In Section II we derive a domain-theoretical model in the spirit of Kittel.[2] Sections III A to III C address the coarsening of the concertina pattern away from the bifurcation, while Sec. III D addresses the stability of the pattern close to the bifurcation. The end of Sec. III is dedicated to a discussion of our theoretical and numerical results from an experimental point of view. In Sec. IV we explain the discretization and the numerical algorithms applied; let us point out that all of the numerical results presented in this paper were obtained from simulations of the reduced model derived in Sec. I H. The rest of the paper is concerned with the effect of anisotropy: We start with the effect of polycrystalline anisotropy and the relationship between the thereby excited ripple and the concertina in Sec. V. Finally Sec. VI deals with different effects of uniaxial anisotropy.

A. The micromagnetic energy

In the experiment under consideration, the variation of the applied magnetic field is on a very slow time scale so that the magnetization always relaxes to equilibrium. Hence our theoretical analysis is based on the micromagnetic (free) energy so that (local) minimizers of the energy correspond to stable configurations in the experiment. Within this model, which was initially introduced in Ref. 3, the magnetization of a ferromagnetic sample occupying some domain Ω is described by a vector field $\mathbf{m}(\mathbf{x}) = (m_1,m_2,m_3)(x_1,x_2,x_3)$; see Fig. 3. (Throughout the paper we employ bold letters to

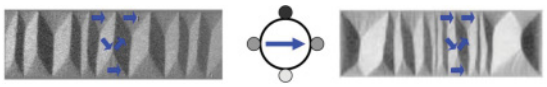

FIG. 1. (Color online) Concertina in a very elongated (length 2 mm) sample of width 50 μm and thickness 50 nm (left) and in a sample of width 35 μm, thickness 40 nm, and moderate length 110 μm (right). The left image shows only the center of the very elongated sample, i.e., less than 10% of the whole sample length. The right image shows an entire sample with its closure domains at the tips. As indicated by the blue arrows, the gray scales encode the transverse component of the magnetization in the domains. Notice that the gray scales in the different pictures are not comparable. In particular the legend in the center has to be understood qualitatively.

denote a vectorial quantity while italic font is used to denote a scalar quantity, in particular some component of a vectorial quantity.)

The micromagnetic energy $E(\mathbf{m})$ is given by

$$E(\mathbf{m}) = d^2 \int_\Omega |\nabla \mathbf{m}|^2 \, d\mathbf{x} + \int_{\text{all space}} |\mathbf{H}_{\text{stray}}|^2 \, d\mathbf{x} - Q \int_\Omega (\mathbf{m}\cdot\mathbf{e})^2 \, d\mathbf{x} - 2 \int_\Omega \mathbf{H}_{\text{ext}} \cdot \mathbf{m} \, d\mathbf{x}. \quad (1)$$

The model in the form of (1) is already partially, i.e., except for lengths, nondimensionalized (for example, the energy itself is rescaled by $K_d = \frac{J_s^2}{2\mu_0}$). The magnetization is rescaled by the saturation magnetization so that $\mathbf{m}$ is a vector field of length 1. Outside of the sample, it vanishes identically:

$$\begin{aligned} |\mathbf{m}|^2 &= 1 \quad \text{in the sample } \Omega, \\ \mathbf{m} &= \mathbf{0} \quad \text{outside of the sample } \Omega. \end{aligned} \quad (2)$$

Let us briefly introduce and discuss the different energy contributions: The first contribution in Eq. (1) is the so-called exchange energy. [The gradient acts componentwise, i.e., $|\nabla \mathbf{m}|^2 = \sum_{i=1}^3 \sum_{j=1}^3 (\partial_i m_j)^2$.] This term favors a uniform magnetization. The material parameter d is called the exchange length and measures the relative strength of exchange with respect to the stray-field energy; see below. It is defined as $d = (\frac{A}{K_s})^{1/2}$, where A denotes the so-called exchange *constant*. The exchange *length* is typically of the order of a few nanometers.

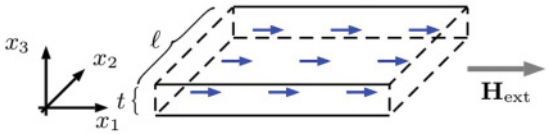

FIG. 3. (Color online) We assume an idealized elongated sample that is infinitely extended or periodic in the direction of the long axis x_1. It is of width ℓ and thickness t. The uniform saturation magnetization $\mathbf{m}^* \equiv (1,0,0)$ is sketched together with the homogeneous external saturation field $\mathbf{H}_{\text{ext}}$ that is applied along the long axis of the sample.

The second contribution in Eq. (1) is the stray-field energy. The static Maxwell equations state that the magnetization $\mathbf{m}$ generates a stray field $\mathbf{H}_{\text{stray}}$ described by

$$\nabla \times \mathbf{H}_{\text{stray}} = \mathbf{0}, \quad \nabla \cdot (\mathbf{H}_{\text{stray}} + \mathbf{m}) = 0, \quad (3)$$

where both equations hold in the whole space and $\mathbf{B} = \mathbf{H}_{\text{stray}} + \mathbf{m}$ is the magnetic induction. Hence the stray field is generated by the divergence of the magnetization. Since the magnetization is discontinuous at the boundary of the sample $\partial\Omega$ [cf. (2)], the second equation in Eq. (3) has to be understood in the following sense:

$$\begin{aligned} \nabla \cdot \mathbf{H}_{\text{stray}} &= \begin{cases} -\nabla \cdot \mathbf{m} & \text{in the sample } \Omega, \\ 0 & \text{outside of the sample } \Omega, \end{cases} \\ [\mathbf{H}_{\text{stray}} \cdot \mathbf{n}] &= \mathbf{m} \cdot \mathbf{n} \quad \text{on the boundary } \partial\Omega, \end{aligned} \quad (4)$$

where $\mathbf{n}$ denotes the outward-pointing normal of the boundary of the sample, and $[\mathbf{H}_{\text{stray}} \cdot \mathbf{n}]$ denotes the jump that $\mathbf{H}_{\text{stray}} \cdot \mathbf{n}$ experiences across the boundary $\partial\Omega$. Hence we distinguish two different sources of the stray field—in analogy to electrostatics one commonly speaks of charges—namely,

magnetic volume charges $\nabla \cdot \mathbf{m}$ in Ω and
magnetic surface charges $\mathbf{m} \cdot \mathbf{n}$ on $\partial\Omega$.

In Sec. I F we discuss specific stray fields that are generated by certain volume or surface charge densities; for further details of how to solve (4) in these cases we refer the reader to Ref. 4. Later on we will also use the following equivalent distributional formulation of (4), which is obtained

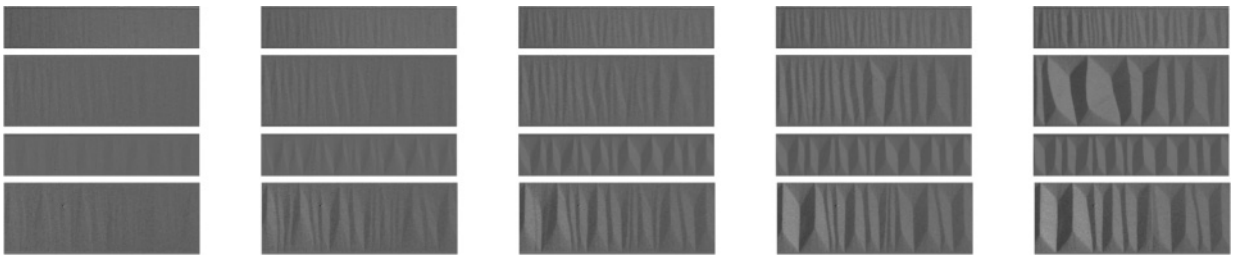

FIG. 2. Formation of the concertina pattern in the experiment: The pictures show a section near the center of the elongated thin-film element. The oscillatory instability grows into a domain-wall pattern which coarsens several times as the strength of the destabilizing field decreases (from left to right). The two upper series show a sample of 30 nm thickness of low anisotropy. The two lower series show a sample of 30 nm thickness of higher anisotropy. The widths are 30 and 50 μm, respectively.

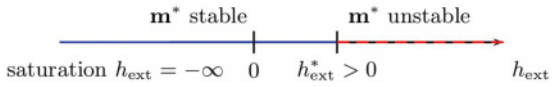

FIG. 4. (Color online) The scale of the external field h_{ext}.

by testing with smooth functions ζ vanishing at infinity, namely,

$$\int_{\text{all space}} \mathbf{H}_{\text{stray}} \cdot \nabla\zeta \, d\mathbf{x} = -\int_{\Omega} \mathbf{m} \cdot \nabla\zeta \, d\mathbf{x}. \tag{5}$$

The third contribution in Eq. (1) models a uniaxial anisotropy, i.e., the preference for an easy axis $\mathbf{e} = (e_1, e_2, e_3)$ in a material. The material parameter $Q > 0$ is called the quality factor. It measures the relative strength of anisotropy with respect to the stray-field energy. A uniaxial anisotropy can, for example, come in the form of crystalline or induced anisotropy. Notice that the polycrystalline anisotropy in a material like Permalloy can be described using a position-dependent easy axis $\mathbf{e}(\mathbf{x})$.

The last contribution in Eq. (1) is called the Zeeman energy. This term models the interaction and favors the alignment of the magnetization with an external magnetic field $\mathbf{H}_{ext}$. It will later turn out to be notationally convenient to parametrize the external field in the form $\mathbf{H}_{ext} = (-h_{ext}, 0, 0)$, so that saturation, i.e., $\mathbf{m} = \mathbf{m}^* \equiv (1,0,0)$, corresponds to large negative values of h_{ext} and so that the instability occurs at a positive value $h_{ext} = h^*_{ext}$; see Fig. 4.

The specific material parameters for our samples can be found in Sec. I D.

B. Previous work and van den Berg's explanation of the concertina

This section contains a comparison to previous work addressing the formation of the concertina pattern and the onset of switching, more precisely nucleation theory, for other sample dimensions and geometries. For a general overview of the theory of magnetic domains we refer to the introductory chapter in Ref. 5. We mention only that first quantitative results were obtained by Kittel[2] based on energy minimization among a reduced set of admissible ansatz functions for the magnetization. He used this so-called domain theory to derive, for example, the typical domain size. It is in principle the same approach that we use for the analysis of the concertina for strong destabilizing fields in Sec. II.

The onset of switching is traditionally analyzed in the framework of so-called nucleation theory. This amounts to a linear stability analysis of a stationary point of the energy, more precisely, the diagonalization of its Hessian. Since the contribution from the exchange energy is diagonal with respect to Fourier cosine *series* whereas the contribution from the stray-field energy is diagonal with respect to the Fourier *transform*, it is typically not possible to determine all eigenmodes and eigenvalues explicitly. Hence it became popular to propose and study specific ansatz functions for the modes—so-called models in the sense of Aharoni[6] (Sec. 9.2.1, p. 189). This allows us to derive an upper bound for the critical field at which the switching begins. We discuss potentially unstable modes in Sec. I F. Our discussion shows that there are at least four qualitatively different regimes for the switching—in terms of the nondimensionalized relative width $\frac{\ell}{d}$ and thickness $\frac{t}{d}$—namely, coherent rotation, buckling, oscillatory buckling, and curling. By a refinement of the discussion in Sec. I F (cf. Theorem 1 in Ref. 7, p. 357), we are even able to show that there are exactly four different parameter regimes for the nucleation. This result contradicts the claim by Aharoni in Ref. 6, p. 200, Sec. 9.4 that there are at most three modes for the nucleation and that buckling plays only a minor role in nucleation. The relevance of oscillatory buckling for the nucleation in elongated thin films was also observed by Usov *et al.*,[8] who investigate elongated thin samples with an elliptical cross section.

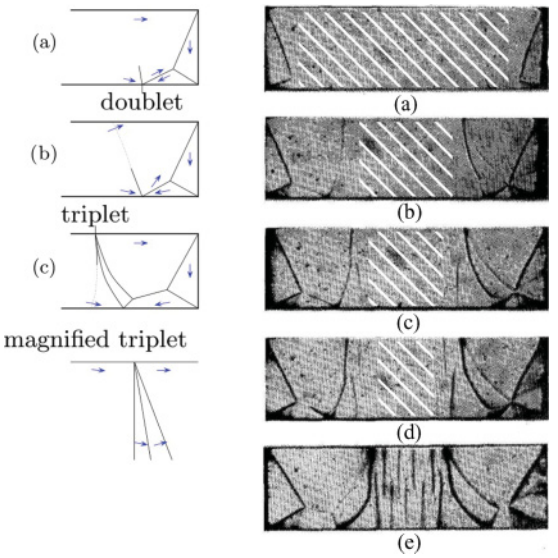

FIG. 5. (Color online) The creation of a triplet (a)–(c) out of the initial doublet as shown and sketched by van den Berg and Vatvani; the sketch is duplicated and the images replicated from Figs. 8 and 9 in Ref. 1. (Reprinted with permission from Ref. 1. Copyright 1981, American Institute of Physics.) The doublet in (a) was created by applying a uniform magnetic field which pushed the central wall of an initial Landau state toward the long edge, where it broke up. The arrows indicate the direction of the magnetization (m_1, m_2). The experimental images (d) and (e) show the buildup process of the concertina via the repeated generation of triplets. The field-penetrated region is hatched.

Before we go on with the discussion of nucleation theory and the mentioned paper[8] we return to van den Berg and Vatvani's paper.[1] In that reference the authors give quite a different explanation for the formation of the concertina in not too elongated samples where the concertina forms by a *successive* outgrowth of the closure domains; see Fig. 5. Combining the explanation of the formation of the concertina pattern therein with the insights from Refs. 9 and 10, we can give the following updated version of the explanation presented in Ref. 1, Secs. A and B: It is a theory about the *two-dimensional mesoscopic* magnetization pattern; by two dimensional, we understand that the magnetization is in plane, i.e., $m_3 = 0$, and independent of the thickness direction, i.e., $\mathbf{m} = \mathbf{m}(x_1, x_2)$; by mesoscopic, we understand that the walls are replaced by sharp discontinuity curves that are charge-free in the sense that the component of the magnetization perpendicular to the wall does not jump; moreover, the magnetization is tangential to the

lateral edges of the sample so that there are no surface charges. In sufficiently large thin-film elements and for sufficiently low external fields, Bryant and Suhl in Ref. 9 postulate that the two-dimensional mesoscopic magnetization pattern arranges itself in such a way that the corresponding continuous magnetic charge density $\sigma = -(\partial_1 m_1 + \partial_2 m_2)$ generates a stray field $\mathbf{H}_{\text{stray}}$ that expels the external field $\mathbf{H}_{\text{ext}}$ from inside the sample (as in electrostatics).

In Ref. 11 (see Ref. 10 for an efficient account), it is shown that in the regime of sufficiently large thin-film elements (i.e., $t \ll \ell$, $\ell t \gg d^2 \ln \frac{\ell}{t}$, and with comparable lateral dimensions of the order $\sim\ell$), this principle extends to moderately large fields (of strength of the order $\sim\frac{t}{\ell}$): In this case, the stray field $\mathbf{H}_{\text{stray}}$ in general can no longer expel the external field $\mathbf{H}_{\text{ext}}$ everywhere in the sample, since the (total) charge density $\sigma = -(\partial_1 m_1 + \partial_2 m_2)$ is limited by $m_1^2 + m_2^2 = 1$.

The charge density σ is then uniquely determined by a *convex* variational problem involving only the stray-field energy and the Zeeman energy. At least some aspects of the mesoscopic two-dimensional magnetization pattern (m_1,m_2) can be recovered from σ: The characteristics of (m_1,m_2), i.e., the curves along which (m_1,m_2) is normal (called trajectories in Ref. 1), have curvature given by σ. However, due to the potential discontinuity curves of the mesoscopic magnetization (m_1,m_2), this seemingly rigid condition does not suffice to determine (m_1,m_2)—even the fact that the discontinuity curves are charge-free is still not enough. Notice that it is easy to construct a particular solution (m_1,m_2) for any charge density σ via the maximal solution of a modified eikonal equation,[10] (p. 2987). On the other hand, in the region where the external field has penetrated, the magnetization (m_1,m_2) is uniquely determined (cf. Ref. 10, p. 2987) and has no discontinuities (cf. Ref. 1, p. 883).

Van den Berg and Vatvani give a recipe for the construction of a solution that corresponds to the experimental observation of a concertina pattern growing out of flux-closure domains at the sample's tips; see Fig. 5. The initial state in his experiments was obtained from an earlier Landau state as the central 180° wall moved toward the edge where it broke up due to the application of a large external field. For sufficiently large external fields [$\mathbf{H}_{\text{ext}} = (-h_{\text{ext}},0,0)$, $h_{\text{ext}} \sim -\frac{t}{\ell}$], $\mathbf{H}_{\text{ext}} + \mathbf{H}_{\text{stray}}$ does not vanish in the sample except in the vicinity of the two distant edges; as a consequence walls occur only in the two flux-closure pattern there. As the external field is reduced the field-penetrated region shrinks as the walls invade the sample. However, the breakup of the central wall of the Landau pattern is not reversible: Each of the two flux-closure patterns has a "doublet," that is, a point on one of the long edges where two wall segments intersect; see Fig. 5(a). The inner doublet walls, i.e., those most distant from the short edges, fade out in the middle (with respect to the long edges) of the cross section; see Fig. 5(a). As the field is reduced these doublets, where the tangential magnetization jumps from left to right, are pinned—at least to some degree. As a consequence, each of the two inner walls grows—necessarily in the direction of the characteristic—till it hits the opposite edge; see Fig. 5(b). There it generates a "triplet," i.e., a point on the edge where three walls meet, which preserves the orientation of the magnetization at the edge of the sample; see the transition from Figs. 5(b) to 5(c). As van den Berg and Vatvani explain at the beginning of Ref. 1, p. 880, the triplet is the simplest wall cluster that preserves the orientation of the magnetization on the boundary of a sample. The middle wall of the triplet must coincide with the previous one originating in the doublet. Again, as the external field is further reduced, the two triplets are essentially pinned, and the inner of the three walls grows toward the opposite edge; see Fig. 5(c).

This process repeats itself [see Fig. 5(d)] until the two half-concertina structures growing from the short edges are linked in the middle (with respect to the short edges) of the cross section; see Fig. 5(e). For very elongated samples of length $L \gg \ell$, the linking takes place at a field strength of order $h_{\text{ext}} \sim -t\ell L^{-2} \ln t\ell^{-1}$—we derive this scaling by calculating the strength of the homogeneous applied magnetic field which can be fully compensated by the stray field of a suitable magnetization configuration—and thus differs from the field at the beginning of the growth process by a factor $\ell^2 L^{-2}$ (up to a logarithm); see above. Speaking in mathematical terms, van den Berg and Vatvani postulate that the positions of doublets and triplets are essentially pinned as the field is decreased, and appeal to continuity, i.e., the pattern should depend continuously on the value of the external field, to overcome the nonuniqueness of (m_1,m_2) mentioned in the second paragraph of this section.

Let us finally discuss the paper by Usov *et al.*[8] in more detail. In this paper, the point is made that in thin films with a sufficiently elongated cross section, nucleation does not take place at the ends of the sample but in the middle, and that it is in the form of an oscillatory buckling instability. This is precisely the type of instability investigated here; cf. Sec. I F. In fact, Ref. 8 allows us to reconcile van den Berg and Vatvani's picture and the picture put forward in this paper on the level of a single geometry, namely, thin films with an elliptical in-plane cross section. In Ref. 8, it is shown by theoretical analysis and numerical simulation that for not-too-elongated elliptical particles, the instability creeps in from the far ends of the cross section, whereas in sufficiently elongated thin films, the instability comes in the form of an oscillatory buckling instability that is most pronounced in the middle of the cross section.

However, there are substantial differences between the analysis in Ref. 8 and ours: The theoretical nucleation analysis in Ref. 8 is based on models of the unstable mode in the sense of Aharoni (Ref. 6, Sec. 9.2.1, p. 189); the model used in Ref. 8 is based on a (truncated) *cosine* series in the direction of the width, i.e., x_2, and thus is not quite suitable to capture edge pinning, i.e., a tangential magnetization also at the lateral edges of the film. Our theoretical nucleation analysis is based on asymptotic modes (cf. Sec. I F; details may be found in Ref. 12, Sec. 3, p. 338); it shows that in the sample-size regime that is of interest to us, the so-called regime III, edge pinning occurs, and the asymptotic unstable mode is a *sine* function in x_2. Moreover, the theoretical nucleation analysis in Ref. 8 predicts a period w^* in x_1 of the unstable mode that is of the order of or larger than the film width ℓ; whereas in regime III, the asymptotic period is given by $(32\pi)^{1/3} d^{2/3} \ell^{2/3} t^{-1/3}$ in line with the experimental observations (cf. Sec. I G). From our point of view, the theoretical analysis in Ref. 8 resides at the boundary between regimes III and II; cf. Sec. I F. Also

the numerical analysis in Ref. 8 is quite different from the one presented here. In Ref. 8, direct numerical simulation of the Landau-Lifschitz-Gilbert equation is used—which limits the nondimensionalized sample widths to $d^{-1}\ell \sim 10$; whereas we derive a reduced model that allows us to treat the sample widths of our experiments, i.e., $d^{-1}\ell$ in the range of 2000 to 20 000.

C. The period of the concertina and the characteristic values of the external field: Van den Berg and Vatvani's vs our predictions

Obviously, our explanation for the formation of the concertina pattern is very different from that of van den Berg and Vatvani. Instead of a *successive* outgrowth (along the sample) of the closure domains, we explain the concertina as a *simultaneous* outgrowth (along the sample) of an unstable mode, best captured in very elongated thin-film elements; see Fig. 2. Indeed, our experiments were performed on thin-film elements of thicknesses t in the range of 10 to 150 nm, widths ℓ in the range of 10 to 100 μm, but lengths L in the range of 2 mm. We recorded the pattern at three different, equidistant sections, i.e., positions $x_1 = L/4, L/2, 3/4L$, and observed qualitatively the same pattern at the same values of the external field.

Not surprisingly, our theoretical predictions are quite different from those in Ref. 1—already in terms of scaling. Van den Berg and Vatvani's explanation entails two different scales of the external field:

(a) $h_{\text{ext}}^{\text{begin}} \sim -\frac{t}{\ell}$ for the beginning of the buildup and

(b) $h_{\text{ext}}^{\text{end}} \sim -t\ell L^{-2} \ln t\ell^{-1}$ for the completion when the external field is totally expelled from the sample.

In our case there is only one characteristic field, namely, the critical field $h_{\text{ext}}^{*} > 0$, at which the simultaneous formation of the concertina throughout the sample due to an interior instability begins—independent of the specific position. (As before and in the following we use an asterisk to denote the critical field in our setting or a specific value of some quantity close to the critical field.) This critical field is given by $h_{\text{ext}}^{*} \sim d^{2/3}\ell^{-4/3}t^{2/3}$ (see regime III in Sec. I F) for isotropic samples—thus since h_{ext}^{*} is positive the instability would occur only after the field is reversed and thus when the van den Berg and Vatvani concertina has already invaded the sample. However, as we discuss later in detail in Sec. VI (linear effect), the critical field is shifted in the case of a transverse anisotropy $h_{\text{ext}}^{*} \rightsquigarrow h_{\text{ext}}^{*} - Q$. It turns out that even for relatively weak transverse anisotropy the shifted critical field is negative and the formation thus starts before the field is reversed. For very elongated samples, i.e., $L \gg \ell$, it holds that $h_{\text{ext}}^{\text{begin}} \gg h_{\text{ext}}^{\text{end}}$, and for the limiting case of an infinitely extended sample $h_{\text{ext}}^{\text{end}} = 0$. The strength of the anisotropy and the geometry of the majority of our samples are such that $h_{\text{ext}}^{\text{begin}} \gg h_{\text{ext}}^{*} \gg h_{\text{ext}}^{\text{end}}$; see Table I. We thus expect and experimentally observe the following scenario in our very elongated samples: At $h_{\text{ext}}^{\text{begin}}$ the van den Berg and Vatvani buildup process starts at the tips of the sample. As the field is reduced, the concertina grows slowly into the sample from the tips. Meanwhile, as h_{ext}^{*} is attained our instability occurs all over the sample—sufficiently far away from the tips and long before the van den Berg and Vatvani linking could take place in the center of the sample; see Table I.

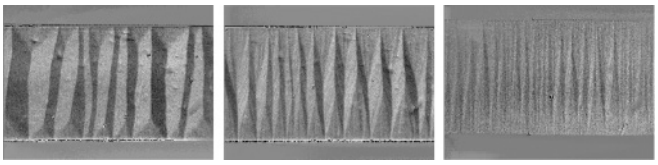

FIG. 6. Concertina in Permalloy samples of width $\ell = 100$ μm and thickness $t = 30$ nm (left), 80 nm (center), and 300 nm (right). Obviously, the average period of the pattern is a decreasing function of the thickness t.

Whereas in van den Berg and Vatvani's theory[1] the appropriate scale for the concertina width w is given by ℓ—in particular independent of the thickness t—it is given by $d^{2/3}\ell^{2/3}t^{-1/3}$ in our case, in qualitative accordance with our experimental observations illustrated in Fig. 6.

D. Experimental setup and samples

In the experiments, we investigated magnetic films of nanocrystalline Permalloy, more precisely $Ni_{81}Fe_{19}$, and amorphous $Co_{60}Fe_{20}B_{20}$, of various thicknesses and induced magnetic anisotropy values. The films were deposited by magnetron sputtering under ultrahigh-vacuum conditions. In order to control the grain growth of the polycrystalline films, a Ta seed (5 nm) layer was used for the $Ni_{81}Fe_{19}$ deposition. In all cases a magnetic in-plane saturation field was applied during film deposition to control the strength and direction of the induced anisotropy. Using different magnetic field histories, films of different effective induced anisotropy were obtained.

(i) A first set of samples was deposited in the presence of a homogeneous, static magnetic field. This results in a maximal

TABLE I. Comparison of the characteristic fields $h_{\text{ext}}^{\text{begin}}$ and $h_{\text{ext}}^{\text{end}}$ in van den Berg and Vatvani's theory of the concertina and the critical field h_{ext}^{*} in our instability for the samples shown in Fig. 2 (thickness $t = 30$ nm, length $L = 2$ mm). Apart from the sample of weak anisotropy and small width (thus less deep in regime III; see Table III), the characteristic fields appear in the expected order, i.e., $h_{\text{ext}}^{\text{begin}} < h_{\text{ext}}^{*} < h_{\text{ext}}^{\text{end}}$.

	$h_{\text{ext}}^{\text{begin}}$	h_{ext}^{*}	$h_{\text{ext}}^{\text{end}}$
	Weak anisotropy ($Q = 1.3 \times 10^{-4}$)		
$\ell = 30$ μm	-1×10^{-3}	4.0×10^{-5}	-1.6×10^{-6}
$\ell = 50$ μm	-6×10^{-4}	-4.2×10^{-5}	-2.8×10^{-6}
	Stronger anisotropy ($Q = 5.0 \times 10^{-4}$)		
$\ell = 30$ μm	-1×10^{-3}	-3.4×10^{-4}	-1.6×10^{-6}
$\ell = 50$ μm	-6×10^{-4}	-4.2×10^{-4}	-2.8×10^{-6}

and also well-aligned induced uniaxial anisotropy. A series of Permalloy and CoFeB samples was obtained by this method.

(ii) In a second set of samples the induced anisotropy was strongly reduced. In order to ensure this, the films were deposited in a magnetic field of alternating orthogonal alignment. The field direction was changed after approximately every 5 nm of film growth. The superposition of the so-obtained orthogonal anisotropy axes results in a strongly reduced induced anisotropy.

The relevant material parameters—for the comparison of the experimental observations to the theoretical predictions—are the following:

(a) The exchange length d for Permalloy is 5 nm and for CoFeB 3 nm.

(b) For both materials the saturation polarization is $J_s \approx 1$ T and the stray-field energy density is given by $K_d \approx 4 \times 10^5$ J/m^3.

(c) The uniaxial anisotropy coefficient is $K_u^{\text{Permalloy}} \approx 200$ J/m^3 for the high-anisotropy Permalloy and $K_u^{\text{CoFeB}} \approx 600$ J/m^3 for CoFeB. For the low-anisotropy Permalloy films we have $K_u^{\text{Permalloy}} \approx 50$ J/m^3.

(d) The quality factor $Q = K_u/K_d$ for high- and low-anisotropy Permalloy is 0.5×10^{-3} and 0.125×10^{-3}, respectively, and for CoFeB is 1.5×10^{-3}.

(e) The average size of the individual grains of Permalloy is assumed to be $\ell_{\text{grain}} \approx 12$–$15$ nm. Moreover, it is assumed that up to a film thickness of about 30 nm, the grains display a columnlike shape. We refer to Refs. 13 and 14 for parameter measurements of similar samples that were deposited using the same sputtering process in the same device.

(f) The film thicknesses range from 10 to 150 nm, the film widths from 10 to 100 μm.

These elongated elements of length 2000 μm were patterned by photolithography and subsequent ion beam etching after film deposition was completed. The elements were aligned, both parallel and orthogonal to the induced anisotropy direction.

The observation of domains and magnetization processes was carried out in a digitally enhanced Kerr microscope; a description of this technique can be found in Ref. 5. The longitudinal Kerr effect was applied with its magneto-optical sensitivity direction transverse to the element axis. The dominant wavelength of the observed concertina patterns was computed by fast Fourier transform. The result of the computation is in agreement with the average wavelength determined by manually counting the folds in the images, as soon as the concertina becomes discernible to the eye during field reduction. The typical strength of the magnetic field, which is applied for saturation at the very beginning, is of the order of some milliteslas.

E. Nucleation

We are interested in the magnetization pattern in elongated thin-film elements of width ℓ (in the x_2 direction) and thickness $t \ll \ell$ (in the x_3 direction) that forms under slow reversal of an external magnetic field aligned with the long axis (the x_1 axis), which is parametrized in the form of $\mathbf{H}_{\text{ext}} = (-h_{\text{ext}},0,0)$; cf. Fig. 3. As mentioned above the minus sign is introduced to simplify the notations so that the critical field in the absence of anisotropy is positive; see below. As mentioned in Sec. I C, we observe no influence of the sample's short edges on the formation of the concertina *away* from the short edges. Since it greatly simplifies the theoretical treatment, we therefore henceforth assume that the sample is infinite in the x_1 direction (and occasionally, for instance in the numerical treatment, impose a large, but artificial period in that direction); see Fig. 3. One consequence of that assumption is that the uniform magnetization $\mathbf{m}^* = (1,0,0)$ is an exact stationary point of the energy functional (1) for *all* values h_{ext} of the external field $\mathbf{H}_{\text{ext}}$ of the form above. Stationarity means that the corresponding Euler-Lagrange equations, which express a torque balance at every point of the sample, are satisfied. The experiments suggest that, as the strength of the field is reduced starting from saturation, i.e., $h_{\text{ext}} < 0$, and finally reversed, a bifurcation at some critical value $h_{\text{ext}}^* > 0$ of the external field $\mathbf{H}_{\text{ext}} = (-h_{\text{ext}},0,0)$ is at the origin of the concertina pattern; see Fig. 2. In the following section we present the outcome of the linear stability analysis. Due to the unit-length constraint (2), infinitesimal variations of $\mathbf{m}^*$ are of the form $\delta\mathbf{m} = (0,\delta m_2,\delta m_3)$. Since the uniform magnetization generates only Zeeman energy, the linearization of the energy in $\mathbf{m}^*$—neglecting anisotropy—is given by the exchange energy and the stray-field energy of the infinitesimal variation, that is, $d^2 \int_\Omega |\nabla\delta\mathbf{m}|^2 d\mathbf{x} + \int_{\text{all space}} |\mathbf{H}_{\text{stray}}(\delta\mathbf{m})|^2 d\mathbf{x}$, augmented by the linearization of the Zeeman energy. The latter is due to the constraint (2) given by $-h_{\text{ext}} \int_\Omega (\delta m_2^2 + \delta m_3^2) d\mathbf{x}$, which is a consequence of the expansion $m_1 = (1 - \delta m_2^2 - \delta m_3^2)^{1/2} \approx 1 - \frac{1}{2}(\delta m_2^2 + \delta m_3^2)$.

F. Unstable modes

We start with the linear stability analysis of the uniform magnetization by discussing potentially unstable modes on the level of the linearization of the energy. Actually, following Aharoni's terminology[6] ([Sec. 9.2.1, p. 189), it would be better to speak of models instead of modes at this point. Nevertheless we proceed in that way since finally our models turn out to be (asymptotic) modes. We consider at which value of the external field h_{ext} each of the modes becomes unstable. At this so-called critical field $h_{\text{ext}} = h_{\text{ext}}^*$, the infinitesimal release of Zeeman energy becomes larger than the infinitesimal contributions due to exchange and stray-field energy. We neglect uniaxial anisotropy (i.e., we set $Q = 0$) for the moment, since on the level of this infinitesimal discussion, a longitudinal or transverse anisotropy just leads to a shift of the critical field (see Sec. VI), $h_{\text{ext}}^* \rightsquigarrow h_{\text{ext}}^* + Q$ or $h_{\text{ext}}^* \rightsquigarrow h_{\text{ext}}^* - Q$, respectively. Since the shift entails that the sign of the critical field can change, we note that if we speak about *reducing* the strength of the external field we usually mean that the critical field is approached from saturation ($h_{\text{ext}} = -\infty$) if not stated differently. Similarly we say that the external field is *increased* after the critical field is passed. In this sense, the critical field is interpreted as the *zero point* on the scale of the external field; cf. Fig. 4.

(I) The first mode we discuss is a coherent rotation, i.e., $\delta\mathbf{m} = (0,\delta m_2,\delta m_3)$ is constant in space; see Fig. 7. Such a mode releases Zeeman energy per length in the x_1 direction of the infinitesimal amount $h_{\text{ext}}\ell t \delta A^2$, where $\delta A = (\delta m_2^2 + \delta m_3^2)^{1/2}$ is the infinitesimal amplitude of the

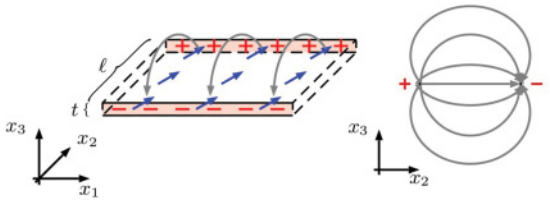

FIG. 7. (Color online) Coherent-rotation perturbation with generated surface charges that act like two oppositely charged wires at distances much larger than t (left). The right image sketches the stray field generated by two oppositely charged wires in the x_2x_3 plane.

coherent rotation. A coherent rotation carries no volume charges but necessarily generates surface charges. Since the top and bottom surfaces have larger area than the two lateral surfaces, an in-plane rotation ($\delta m_3 \equiv 0$) is favored. This mode generates surface charges of infinitesimal density $\pm\delta A$. Over distances much larger than t, these surface charges act like two oppositely charged wires at distance ℓ with line charge density $t\delta A$—also in the following if not mentioned otherwise always infinitesimally and per length in the x_1 direction. Due to dipolar interaction of the opposite surface charges, the stray field essentially extends up to distances $\sim\ell$ away from the sample. Therefore the dominant contribution to the energy stems from the near stray field. It is given as the sum of the fields of each of the "charged wires." These fields scale and decay as $\sim t\delta A r^{-1}$ over distances r smaller than ℓ and larger than t from the center of the wire. Integrating the superimposed near stray fields of each of the oppositely charged wires, we obtain that the coherent-rotation mode generates an infinitesimal stray field of order $\sim t^2(\ln \ell t^{-1})\delta A^2$. Therefore, this mode becomes unstable when $h_{\rm ext} \sim t\ell^{-1}(\ln \ell t^{-1})$. We note that this is the mode considered in the Stoner-Wohlfarth model.[15]

(II) The second mode we consider is buckling; see Fig. 8. In this case the magnetization avoids the lateral surface charges by just laterally buckling in the middle of the cross section, i.e., $\delta\mathbf{m} = (0,\delta A \sin(\pi \frac{x_2}{\ell}),0)$. However, since $\nabla\cdot\delta\mathbf{m} = \pi\ell^{-1}\delta A\cos(\pi\frac{x_2}{\ell})$, the surface charges of the coherent rotation turn into volume charges. At distances much larger than t from the cross section, these volume charges act like surface charges on a plate of amplitude $\sim\ell^{-1}t\delta A$. Since these surface charges change sign over a distance ℓ, they generate a stray field which essentially extends a distance $\sim\ell$ away from the cross section,

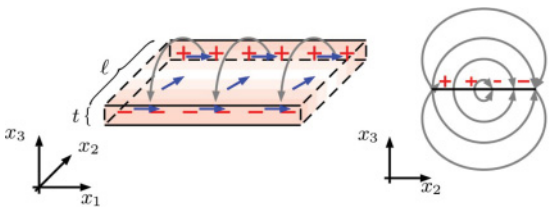

FIG. 8. (Color online) Buckling mode with generated density of volume charges, which act like surface charges on a plate at distances much larger than t, and the generated stray field. For reasons of a clear presentation the field is drawn only in the region above the sample (left). The right image shows an x_2x_3 section of the stray field generated by the surface-charge density on the plate (independent of x_1) that changes sign over distance ℓ with respect to x_2. The stray field extends roughly a distance ℓ from the sample into space.

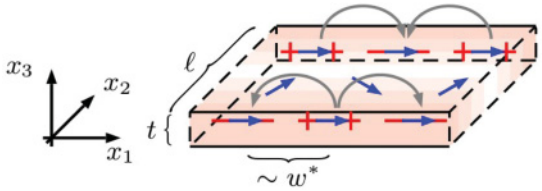

FIG. 9. (Color online) Oscillatory buckling mode and generated surface charges and stray field—for reasons of clarity drawn only in the region above the sample. Compared to Fig. 8, the opposite charges are now at closer distance w^*, so that the stray field extends roughly only a distance w^* into space. Moreover, the dominant components of the stray field are h_1 and h_3.

as in the case of mode I. We note that a surface charge distribution on a plate generates a field whose jump across the plate is given by the charge density itself. One hence obtains that the stray field is of the form $\sim\ell^{-1}t\delta A g(x\ell^{-1})$, for some generic function g, i.e., a function g that is independent of the parameters under consideration. Hence the buckling mode generates a stray-field energy $\sim t^2\delta A^2$, which is smaller only by a logarithm than in the case of the previous mode of coherent rotation. Moreover, since $|\nabla\delta\mathbf{m}|^2 = \pi^2\ell^{-2}\delta A^2\cos^2(\pi\frac{x_2}{\ell})$, the mode generates exchange energy $\sim d^2\ell^{-1}t\delta A^2$. Since the release of Zeeman energy scales as $\sim h_{\rm ext}\ell t\delta A^2$ as in the case of the first mode above, this mode becomes unstable at $h_{\rm ext} \sim d^2\ell^{-2}$ in the regime $t \ll d^2\ell^{-1}$ and at $h_{\rm ext} \sim t\ell^{-1}$ in the regime $t \gg d^2\ell^{-1}$.

Let us point out that the difference in stray-field energy between the two modes I and II comes from the different behavior of the near stray field: In the case of the buckling mode, the stray-field energy is (slightly) smaller since opposite charges are distributed toward the center of the sample and thus are closer together. This leads to a smaller near stray field as compared to coherent rotation where the charges are well separated at distance ℓ.

(III) The third mode we discuss is oscillatory buckling; see Fig. 9. This mode further reduces the stray-field energy through a modulation of the lateral buckling in the x_1 direction, i.e., $\delta\mathbf{m} = (0,\delta A\sin(\pi\frac{x_2}{\ell})\sin(2\pi\frac{x_1}{w}),0)$ with a wavelength w that satisfies $t \ll w \ll \ell$. Since $w \gg t$, the volume charges generated by this mode act like surface charges of amplitude $\sim\ell^{-1}t\delta A$ over distances much larger than t from the cross section. However, these surface charges change sign over a distance $w \ll \ell$, so that the generated stray field extends only over a distance $\sim w$ away from the cross section. Hence this mode generates a stray-field energy $\sim\ell^{-1}t^2w\delta A^2$, which is substantially less than the stray-field energy of the two prior modes for $w \ll \ell$. However, since $w \ll \ell$, the exchange energy is now dominated by the oscillation in the x_1 direction, which leads to an infinitesimal exchange energy $\sim d^2\ell w^{-2}t\delta A^2$. Hence the wavelength w which leads to the minimal infinitesimal total stray-field energy and exchange energy of order $\sim d^{2/3}\ell^{-1/3}t^{5/3}\delta A^2$ is given by $w^* \sim d^{2/3}\ell^{2/3}t^{-1/3}$. This is consistent with our assumption $t \ll w \ll \ell$ provided $d^2\ell^{-1} \ll t \ll (d\ell)^{1/2}$. The oscillatory buckling mode becomes unstable at a field strength of order $h_{\rm ext} \sim d^{2/3}\ell^{-4/3}t^{2/3}$.

(IV) The fourth mode we consider is curling. This mode avoids charges altogether by an x_3-dependent magnetization, i.e., $\delta\mathbf{m} = (0,\delta A\sin(\pi\frac{x_2}{\ell})\cos(\pi\frac{x_3}{t}),$ $\delta A\ell^{-1}t\cos(\pi\frac{x_2}{\ell})\sin(\pi\frac{x_3}{t}))$. The exchange energy in this

TABLE II. Overview of the four different regimes and the corresponding scaling of the critical field.

Regimes I–IV	h^*_{ext}(modes I–IV)
$\frac{t}{d} \ll (\frac{\ell}{d})^{-1} \ln^{-1}[(\frac{\ell}{d})^{-1}]$	$\sim t\ell^{-1}(\ln \ell t^{-1})$
$(\frac{\ell}{d})^{-1} \ln^{-1}[(\frac{\ell}{d})^{-1}] \ll \frac{t}{d} \ll (\frac{\ell}{d})^{-1}$	$\sim d^2\ell^{-2}$
$(\frac{\ell}{d})^{-1} \ll \frac{t}{d} \ll (\frac{\ell}{d})^{1/2}$	$\sim d^{2/3}\ell^{-4/3}t^{2/3}$
$(\frac{\ell}{d})^{1/2} \ll \frac{t}{d} \ll \frac{\ell}{d}$	$\sim d^2t^{-2}$

case is dominated by the gradient in the x_3 direction, which scales as $\sim d^2\ell t^{-1}\delta A^2$. Hence the curling mode becomes unstable at $h_{\text{ext}} \sim d^2t^{-2}$.

The discussion above shows that there are (at least) four different parameter regimes for the nucleation, expressed in terms of the two nondimensional parameters $t/d \ll \ell/t$; see Table II. The regimes are characterized by a certain scaling of the critical field $h^*_{\text{ext}}(\frac{t}{d}, \frac{\ell}{d})$ in the sense that one of the modes becomes unstable as the external field passes the corresponding field, while the other three modes are still stable; see Fig. 10. In particular, the oscillatory buckling mode is the first mode to become unstable at a field $h^*_{\text{ext}} \sim d^{2/3}\ell^{-4/3}t^{2/3}$ in the regime $d^2\ell^{-1} \ll t \ll (d\ell)^{1/2}$, i.e., $h^*_{\text{ext}}(\text{mode III}) < \min\{h^*_{\text{ext}}(\text{mode I}), h^*_{\text{ext}}(\text{mode II}), h^*_{\text{ext}}(\text{mode IV})\}$. Note that the different scalings of h^*_{ext} pairwise coincide at the crossover between two regimes.

We finally point out that a refinement of the above discussion rigorously shows that there are exactly four regimes; cf. Theorem 1 in Ref. 7, p. 357. Hence, in the sense of Aharoni the four models turn out to be asymptotic modes.

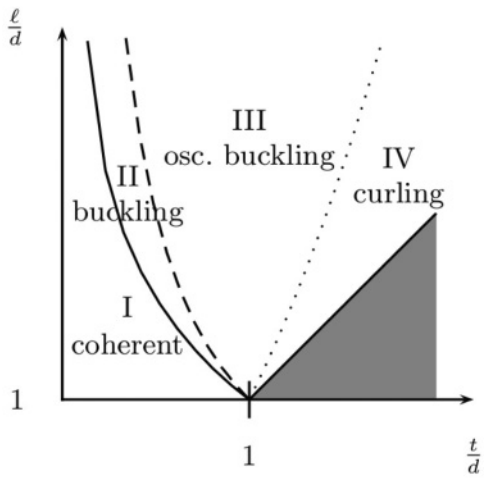

FIG. 10. Phase diagram for the four regimes for nucleation. The boundaries of the different regimes are obtained from Table II by representing ℓ/d as a function of t/d at the regime boundaries; for example, the boundary between regimes III and IV is then given by the graph $\ell/d = (t/d)^2$. Inside each region the corresponding mode is the first mode to become unstable, i.e., the corresponding strength of the critical field of the mode is smaller than the strength for the other three modes. The shaded region corresponds to samples whose thickness t is larger than their width ℓ.

TABLE III. Parameters $\epsilon = d^2\ell^{-1}t^{-1}$ and $\delta = d^{-1/2}\ell^{-1/2}t$ characterizing regime III for typical sample sizes where the exchange length is given by $d = 5$ nm. Regime III is equivalent to $\epsilon \ll 1$ and $\delta \ll 1$. For our samples this is simultaneously best matched for $\ell = 150\ \mu$m and $t = 10$ nm.

ℓ t	10 nm	150 nm
10 μm	$\epsilon = 0.25 \times 10^{-3}$	$\epsilon = 0.0167 \times 10^{-3}$
	$\delta = 0.0447$	$\delta = 0.6708$
100 μm	$\epsilon = 0.025 \times 10^{-3}$	$\epsilon = 0.0017 \times 10^{-3}$
	$\delta = 0.0141$	$\delta = 0.2121$

G. Period of the unstable mode: Experiment vs theory

Clearly, the regime of interest for us is regime III, i.e., the oscillatory buckling regime characterized by $d^2\ell^{-1} \ll t \ll (d\ell)^{1/2}$; see Table III. In this regime, an asymptotic analysis of the linearization of the energy on the basis of the above discussion shows that the (first) unstable mode is indeed asymptotically of the form

$$\delta\mathbf{m} = \left(0, \delta A \sin\left(\pi \frac{x_2}{\ell}\right) \sin\left(2\pi \frac{x_1}{w}\right), 0\right); \tag{6}$$

cf. Theorem 1 in Ref. 12, p. 389, and see also below. Based on a refinement of the prior linear stability analysis, one can confirm the asymptotic behavior of w^* and determine in addition the numerical factor given by

$$w^* \approx (32\pi)^{1/3} d^{2/3}\ell^{2/3}t^{-1/3}. \tag{7}$$

So far we have learned that in regime III at field strengths $h^*_{\text{ext}} \sim d^{2/3}\ell^{-4/3}t^{2/3}$ there is a bifurcation in the direction of the unstable mode $\delta\mathbf{m} = (0, \delta A \sin(\pi \frac{x_2}{\ell}) \sin(2\pi \frac{x_1}{w^*}), 0)$. We claim that the concertina pattern grows out of this unstable mode. If so, the experimentally observed period w^*_{expt} should be close to the period w^* of the unstable mode. Defining and determining w^*_{expt} are delicate: As h_{ext} increases (after the critical field h^*_{ext} is passed), there is usually a continuous transition from the magnetization ripple (see Sec. V) to the concertina pattern, which is far from exactly periodic, and which coarsens subsequently (see Sec. III). As w^*_{expt} we take the average period as soon as the concertina pattern is discernible to the eye. Figure 11 shows the result of this comparison for a broad range of sample dimensions ℓ and t and (therefore) a fairly broad range of periods w^*: The ratio of the smallest width ℓ compared to the largest is 5; the ratio of the smallest thickness t compared to the largest is 15. The smallest period w^* is expected for a thick film of small width, the largest period for a thin film of large width, differing by a factor close to 6 (neglecting the prediction for broken or defective samples); cf. Fig. 11, bottom. The ratio $\frac{w^*_{\text{expt}}}{w^*}$ of the experimental period with respect to the prediction ranges around 2; cf. Fig. 11, top. We basically see this as a confirmation of our hypothesis, namely, that the concertina grows out of the oscillatory buckling. Notice that the deviation has a clear trend: w^*_{expt} is larger than w^*. We give an explanation for this systematic deviation in Sec. III.

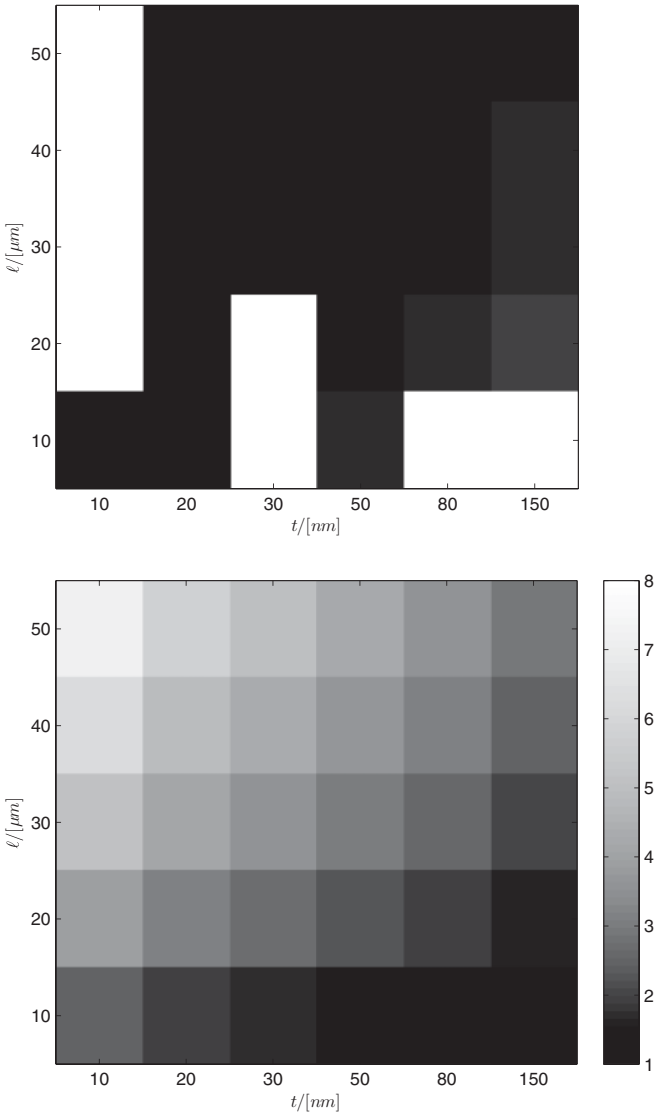

FIG. 11. The theoretical period of the unstable mode is in good agreement with the measurements: The upper image shows the ratio of the experimentally observed period and the period of the unstable mode. The white patches correspond to broken or defect-ridden samples. The lower displays the ratio of the period w^* and the smallest period at all, i.e., $w^*(\ell = 50\ \mu\text{m}, t = 150\ \text{nm})$. Both images share the same color map (grayscale).

H. A reduced energy functional

In the forthcoming section we start with an investigation of the type of bifurcation. For the moment we continue to neglect anisotropy, although it may affect the type of bifurcation as we shall discuss in Sec. VI. In order to understand the type of bifurcation we now first pass to a reduced model adapted to our regime III: The form of the unstable mode suggests that the out-of-plane component and the dependence on the thickness variable are negligible, i.e., we assume $m_3 \equiv 0$ and $\mathbf{m} = \mathbf{m}(x_1,x_2)$, respectively. Since the unstable mode varies faster in the x_1 direction than in the x_2 direction, we neglect $|\partial_2 \mathbf{m}|^2$ with respect to $|\partial_1 \mathbf{m}|^2$ in the exchange energy density. Since the oscillation in the sign of the charge density is on smaller length scales in the x_1 direction than in the x_2 direction, we neglect h_2^2 with respect to $h_1^2 + h_3^2$ in the stray-field energy density, where $\mathbf{H}_{\text{stray}} = (h_1,h_2,h_3)$. Finally, since we are interested in small deviations from $\mathbf{m}^* = (1,0,0)$, we expand $m_1 = \sqrt{1 - m_2^2} \approx 1 - \frac{m_2^2}{2}$, so that we may neglect $|\nabla m_1|^2$ with respect to $|\nabla m_2|^2$ in the exchange energy density. We also use this approximation in the charge density and in the Zeeman energy. Hence (up to an additive constant) we are left with the *reduced energy*

$$E_0(m_2) \approx d^2 t \int_{\Omega'} (\partial_1 m_2)^2 dx_1 dx_2 + \int_{\text{all space}} \left(h_1^2 + h_3^2\right) \times dx_1 dx_2 dx_3 - h_{\text{ext}} t \int_{\Omega'} m_2^2\, dx_1 dx_2, \tag{8}$$

where the stray field $\mathbf{H}_{\text{stray}} = (h_1,0,h_3)$ is determined via

$$\partial_3 h_1 - \partial_1 h_3 = 0, \tag{9}$$

$$\int_{\text{all space}} (h_1 \partial_1 \zeta + h_3 \partial_3 \zeta) dx_1 dx_2 dx_3 = t \int_{\Omega'} \left(-\frac{m_2^2}{2} \partial_1 \zeta + m_2 \partial_2 \zeta\right) dx_1 dx_2 \quad \text{for all } \zeta. \tag{10}$$

Notice that (9) is just the condition that the stray field is rotation-free for a stray field independent of x_2 with vanishing x_2 component [cf. (3)], while (10) is a consequence of the alternative formulation (5). Here, Ω' denotes the in-plane cross section of our sample, $\Omega = \Omega' \times (0,t)$.

We note that the stray-field energy is finite only if m_2 vanishes at the lateral long edges, i.e., $m_2(x_1,x_2) = 0$ for $x_2 = 0,\ell$ (as is true for the unstable mode). Notice that (9) and (10) can be written as

$$\begin{aligned} \partial_1 h_1 + \partial_3 h_3 = 0 \quad & \text{for } x_3 \neq 0, \\ [h_3] = t\left(-\partial_1 \frac{m_2^2}{2} + \partial_2 m_2\right) \quad & \text{for } x_3 = 0, \end{aligned} \tag{11}$$

where $[h_3]$ denotes the jump h_3 experiences across $x_3 = 0$. This formulation shows that x_2 is just a parameter in the equations for the stray field, which behaves like a two-dimensional stray field in the corresponding x_1x_3 plane generated by the charge density $t(-\partial_1 \frac{m_2^2}{2} + \partial_2 m_2)$ that amounts to a "line charge" in the corresponding x_1x_3 plane.

Furthermore, the only nonquadratic term in the energy comes from the nonlinear charge distribution $t(-\partial_1 \frac{m_2^2}{2} + \partial_2 m_2)$. This allows us to derive the scaling of the amplitude of the magnetization: It should be such that both terms in the charge distribution balance. Since in view of the unstable mode the typical x_1 scale of variations of m_2 is given by $w^* \sim d^{2/3}\ell^{2/3}t^{-1/3}$, whereas the typical x_2 scale of variations of m_2 is given by the sample width ℓ, the contributions $\partial_1 \frac{m_2^2}{2}$ and $\partial_2 m_2$ balance, provided the amplitude of m_2 scales as $d^{2/3}\ell^{-1/3}t^{-1/3}$. This suggests the following nondimensionalization of length and reduced units for the stray field and the magnetization:

$$\begin{aligned} x_1 &= d^{2/3}\ell^{2/3}t^{-1/3}\hat{x}_1, \quad x_2 = \ell\hat{x}_2, \quad x_3 = d^{2/3}\ell^{2/3}t^{-1/3}\hat{x}_3, \\ h_1 &= d^{2/3}\ell^{-4/3}t^{2/3}\hat{h}_1, \quad h_3 = d^{2/3}\ell^{-4/3}t^{2/3}\hat{h}_3, \\ m_2 &= d^{2/3}\ell^{-1/3}t^{-1/3}\hat{m}_2. \end{aligned} \tag{12}$$

The scaling of the space variable x_3 was chosen as the typical length scale of the stray field in the ambient space and not as

the sample's thickness so that the condition that the stray field is rotation-free (9) is inherited. The scaling for the stray field is just the one that we obtained in the discussion of the oscillatory buckling mode in Sec. I F. We also rescale the external field using the scaling of the critical field obtained in the discussion of the oscillatory buckling mode:

$$h_{\text{ext}} = d^{2/3}\ell^{-4/3}t^{2/3}\hat{h}_{\text{ext}}, \tag{13}$$

The energy itself is rescaled using the scaling of the energy density that is obtained from the same discussion so that the rescaled energy becomes independent of $\frac{\ell}{d}$ and $\frac{t}{d}$:

$$E = d^{8/3}\ell^{-1/3}t^{2/3}\hat{E}_0. \tag{14}$$

Hence we obtain the reduced rescaled energy functional

$$\hat{E}_0(\hat{m}_2) = \int_{\hat{\Omega}'} (\hat{\partial}_1\hat{m}_2)^2 d\hat{x}_1 d\hat{x}_2 + \int_{\text{all space}} \left(\hat{h}_1^2 + \hat{h}_3^2\right) d\hat{x}_1 d\hat{x}_2 d\hat{x}_3 - \hat{h}_{\text{ext}} \int_{\hat{\Omega}'} \hat{m}_2^2 d\hat{x}_1 d\hat{x}_2. \tag{15}$$

The reduced rescaled stray field is determined by

$$\hat{\partial}_1\hat{h}_1 + \hat{\partial}_3\hat{h}_3 = 0 \quad \text{for } \hat{x}_3 \neq 0,$$
$$[\hat{h}_3] = \left(-\hat{\partial}_1\frac{\hat{m}_2^2}{2} + \hat{\partial}_2\hat{m}_2\right) \quad \text{for } \hat{x}_3 = 0.$$

The reduced rescaled formulation shows that the reduced energy functional contains just one nondimensional parameter, namely, the reduced external field $\hat{h}_{\text{ext}}$, instead of four parameters (exchange length, sample dimensions, and h_{ext}) for the full model. Moreover, the vector field $\mathbf{m} = (m_1, m_2, m_3)$, a function of three variables (x_1, x_2, x_3), has been replaced by the scalar function $\hat{m}_2$, a function of two variables $(\hat{x}_1, \hat{x}_2)$. Finally, the computation of the stray field is a two-dimensional computation [in $(\hat{x}_1, \hat{x}_3)$ only, with $\hat{x}_2$ as a parameter] instead of a three-dimensional one. All this simplifies both the theoretical treatment and the numerical simulation. For clarity, we will mostly discuss our results in the rescaled variables (15)—and only occasionally return to the original variables, mostly for comparison with the experiment, for which all quantitative results have to be reexpressed in the original variables, and when we take into account anisotropy.

In Theorem 3 in Ref. 16, p. 233, we rigorously show that the reduced energy functional is the scaling limit of the renormalized full micromagnetic energy in regime III.

I. Bifurcation

We now return to the issue of the type of bifurcation on the level of the reduced model. In contrast to the three-dimensional micromagnetic energy, the Hessian of the reduced model in $\hat{m}_2 \equiv 0$—which corresponds to the uniform magnetization $\mathbf{m} \equiv (1,0,0)$ in the full model—can be explicitly diagonalized, and the first unstable mode is given by $\hat{m}_2^* = \sin(\pi\hat{x}_2)\sin(2\pi\frac{x_1}{\hat{w}^*})$, where $\hat{w}^* = (32\pi)^{1/3}$ in agreement with (6) and (7). The reduced critical field is given by

$$\hat{h}_{\text{ext}}^* = 3\left(\frac{\pi}{2}\right)^{4/3}. \tag{16}$$

In order to determine the type of bifurcation, we have to investigate the energy functional $\hat{E}_0$ close to the one-dimensional subspace $\{A\hat{m}_2^*\}$ generated by the unstable mode $\hat{m}_2^*$. Because of the invariance of both the energy $\hat{E}_0$ and the unstable mode $\hat{m}_2^*$ under the transformation ($\hat{m}_2 \rightsquigarrow -\hat{m}_2$ and $\hat{x}_2 \rightsquigarrow 1 - \hat{x}_2$), all odd terms in the amplitude A in the expansion of $\hat{E}_0(A\hat{m}_2^*)$ vanish. In particular the cubic term vanishes so that the bifurcation is degenerate.

This degeneracy of the bifurcation means that, at the critical field strength $\hat{h}_{\text{ext}}^*$, the first nonvanishing term in the expansion of $\hat{E}_0(A\hat{m}_2^*)$ with respect to A is at least quartic. Hence it is not sufficient to consider $\hat{E}_0$ restricted to the linear space $\{A\hat{m}_2^*\}$; it has to be analyzed along a curve $\{A\hat{m}_2^* + A^2\hat{m}_2^{**}\}$ in configuration space. Indeed, the curvature direction $\hat{m}_2^{**}$ affects the quartic term in the expansion and has to be determined such that $\hat{E}_0$ is minimal. This minimization problem of the coefficient of the quartic term is quadratic in $\hat{m}_2^{**}$ and thus can be solved explicitly. We obtain

$$\hat{m}_2^{**} = -\frac{1}{10}\left(\frac{2}{\pi}\right)^{1/3}\sin(2\pi x_2)\sin\left(4\pi\frac{x_1}{\hat{w}^*}\right),$$

which leads to a negative coefficient of the quartic term in the expansion of $\hat{E}_0$, namely,

$$\hat{E}_0(A\hat{m}_2^* + A^2\hat{m}_2^{**}) \approx (\hat{h}_{\text{ext}} - \hat{h}_{\text{ext}}^*)\left(\frac{\pi}{2}\right)^{1/3}A^2 - \frac{\pi}{640}A^4. \tag{17}$$

The negative quartic coefficient implies that the bifurcation is subcritical or of first order. Subcriticality entails that close to $\hat{m}_2 \equiv 0$ there are only *unstable* stationary points for $\hat{h}_{\text{ext}}$ slightly below $\hat{h}_{\text{ext}}^*$, and no stationary points close to $\hat{m}_2 \equiv 0$ for $\hat{h}_{\text{ext}}$ slightly above $\hat{h}_{\text{ext}}^*$; see Fig. 12.

At first sight it is surprising that the stray-field energy contribution to $\hat{E}_0$, which gives rise to the only quartic term in $\hat{m}_2$, and clearly is non-negative, may nevertheless allow for a negative coefficient in front of the quartic term in the expansion (17). This comes from the fact that the two terms in the charge density $-\hat{\partial}_1\frac{\hat{m}_2^2}{2} + \hat{\partial}_2\hat{m}_2$ interact, giving rise to a cubic term in $\hat{m}_2$ (quartic in A), which indeed allows for cancellations. The way in which this operates is better understood in physical space: The term $\hat{m}_2^{**}$ in $A\hat{m}_2^* + A^2\hat{m}_2^{**}$ (the curvature direction in configuration space) induces a tilt of the symmetric charge distribution of $A\hat{m}_2^*$; see Fig. 13. This tilt brings opposite charges closer together, thereby reducing the stray-field energy—while increasing the exchange energy to a lesser amount.

Since the bifurcation is first order, it is not obvious whether minimizers of the reduced energy functional can be related to the unstable mode. In particular, this finding sheds doubt on our hypothesis that the concertina pattern inherits the period of

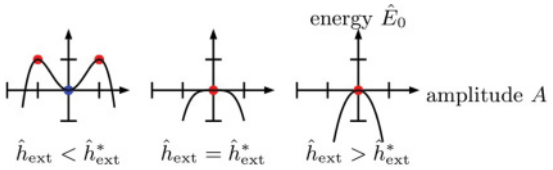

FIG. 12. (Color online) Energy landscape close to the bifurcation. The loss of stability at the critical field leads to a first-order phase transition—on a large scale, however, the energy is coercive.

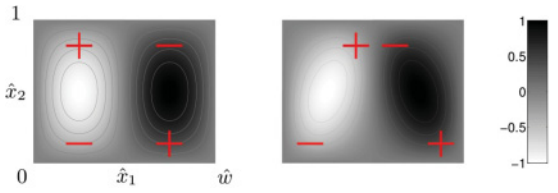

FIG. 13. (Color online) Unstable mode $\{\hat{m}_2^*\}$ and additional curvature correction $\{A\hat{m}_2^* + A^2\hat{m}_2^{**}\}$, $A = 0.1$, with generated charges on the domain $[0,\hat{w}^*) \times (0,1)$. The values are normalized by the maximum so that the grayscale reaches from -1 to 1.

the unstable mode. It is not even obvious whether minimizers of the reduced energy functional exist at all. However, one can show that the reduced energy is coercive for all values of the external field $\hat{h}_{\text{ext}}$; see Theorem 4 in Ref. 16, p. 236. This implies that there always exists a global minimizer of the reduced energy—which corresponds to a local minimizer of the original energy (1); see Theorem 5 in Ref. 16, p. 237—in particular for fields larger than the critical field. But it is not immediately clear how these minimizers relate to the unstable mode.

It is natural to resort to numerical simulations; details on the discretization and the algorithms are provided in Sec. IV. To confirm the conjecture that the unstable mode in regime III is indeed related to the concertina pattern, we use a numerical path-following algorithm in order to compute the bifurcation branch. Figure 14 shows the outcome

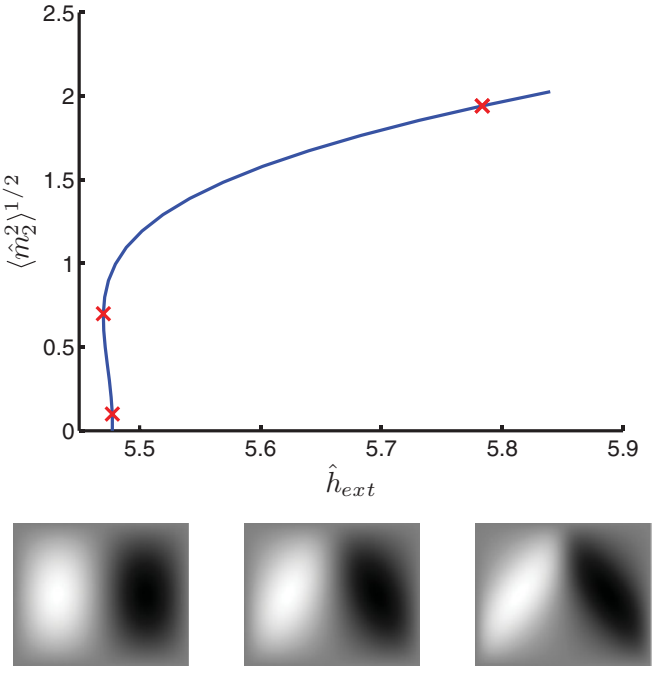

FIG. 14. (Color online) Numerical simulations: The $\hat{w}^*$-periodic branch close to the bifurcation and the pattern at the indicated fields (increasing average amplitude $\langle \hat{m}_2^2 \rangle^{1/2}$ from left to right). By $\langle \hat{m}_2^2 \rangle^{1/2}$ we denote the spatial root mean square of $\hat{m}_2$, i.e., the amplitude of the average magnetization. The grayscales encode the m_2 component but are not comparable. The whole spectrum is considered so that the structure of the pattern can best be resolved; bright regions correspond to $\hat{m}_2 < 0$, dark regions to $\hat{m}_2 > 0$. The computational domain is $\hat{\Omega} = [0,\hat{w}) \times [0,1]$.

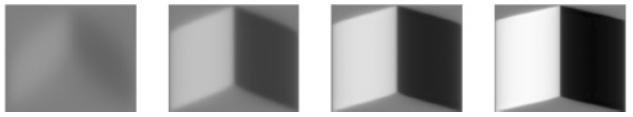

FIG. 15. Numerical simulations: The $\hat{w}^*$-periodic concertina pattern exhibits a clear scale separation as $\hat{h}_{\text{ext}}$ increases; $\hat{h}_{\text{ext}} = 6.84, 23.2, 40.1, 57.3$ from left to right. The grayscales linearly encode the $\hat{m}_2$ component and are comparable. The computational domain is $\hat{\Omega} = [0,\hat{w}) \times [0,1]$.

of the numerical simulations. As expected, due to the coercivity of the energy functional, we find a turning point as we follow the bifurcation branch. The turning point is located at a field which is just slightly—about 1%—smaller than the critical field. After the turning point the configurations become stable, at least under perturbations of the same period.

As the field increases beyond the turning point, the unstable mode develops into a domain pattern of concertina type with its typical scale separation between the wall width and the domain size; see Fig. 15. We thus find a continuous transition from the unstable mode to the concertina pattern, confirming our hypothesis.

We recall that in order to compare the computed configurations to the experiment one first has to redo the rescaling of length, magnetization, and the external field as in Eq. (12) and (13) using the particular sample dimensions ℓ and t and the exchange length d. Due to the anisotropic rescaling of x_1 and x_2, this will in particular change the angles of the configuration. Notice also that in the oscillatory buckling regime $[d^2\ell^{-1} \ll t \ll (d\ell)^{1/2}]$ values of the order of $\hat{m}_2 \sim 1$ will turn into $m_2 \ll 1$, since $d^{2/3}\ell^{-1/3}t^{-1/3} \ll 1$ is equivalent to the lower bound characterizing regime III; see (12) and Table III. In principle, the grayscales of the configurations which encode the transverse component of the magnetization could also be compared to the grayscales in the experiment. However, quantitative processing is involved and is beyond the scope of the present work.

The numerical simulations lead to the conjecture that the magnetization in a perfectly homogeneous, isotropic sample exhibits a first-order phase transition from the uniformly magnetized state to the concertina state of period w^* at the critical field. Clearly this does not explain the systematic deviation of the average wavelength in the experimental measurements from the theoretical prediction. Before we address this deviation we now introduce a sharp-interface model, so-called *domain theory*, that is used to investigate the further transformation of the concertina for large external fields $\hat{h}_{\text{ext}} \gg 1$, in particular its coarsening; see Secs. III A, III B, and III C. Our explanation of the coarsening will also provide an understanding of the initial deviation of the period; see Sec. III D.

II. DOMAIN THEORY

In the numerical simulations, we observe for large external fields a clear scale separation between domains, where the magnetization is almost constant, and walls, in which the magnetization quickly turns; cf. Fig. 15. This suggests the application of a sharp-interface model, namely, domain theory. In the following we first discuss admissible ansatz functions

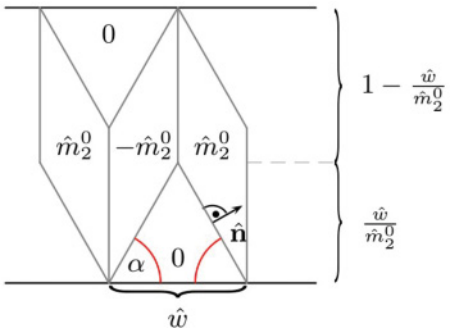

FIG. 16. (Color online) Domain theory: The mesoscopic charge-free ansatz function.

and then derive their energy within domain theory. This leads to a model which depends on only a small number of parameters in configuration space; the model is used in Secs. III and VI in order to get a better understanding of the coarsening of the concertina. The application of such an approach dates back to Kittel[2] who could thereby already estimate characteristic length scales of domain patterns.

On a mesoscopic scale, the computed magnetization is close to a piecewise constant magnetization of amplitude $\hat{m}_2^0$, i.e., $\hat{m}_2 = \pm\hat{m}_2^0$ in the quadrangular domains and $\hat{m}_2 = 0$ in the triangular domains, as indicated in Fig. 16. We observe that the angles in the pattern are related to the amplitude of the magnetization $\hat{m}_2^0$ (cf. Fig. 15); approximately we have that $\tan\alpha = 2\hat{m}_2^0$. This is related to the fact that the (reduced) stray-field energy is strongly penalized for large fields, as we shall explain now. In fact, the piecewise-constant magnetization of that form is a distributional solution of

$$-\hat{\partial}_1\left(\frac{\hat{m}_2^2}{2}\right) + \hat{\partial}_2\hat{m}_2 = 0, \tag{18}$$

which means that the normal component of the vector field $(-\frac{\hat{m}_2^2}{2},\hat{m}_2)$ is continuous across the interfaces—this is a version of the Rankine-Hugoniot condition in the theory of conservation laws. This condition obviously holds in the case of vertical walls. In the case of diagonal walls the condition

$$0 = \left[\hat{\mathbf{n}}\cdot\left(-\frac{\hat{m}_2^2}{2},\hat{m}_2\right)\right] = \hat{\mathbf{n}}\cdot\left(-\frac{1}{2}\left(\hat{m}_2^0\right)^2,\hat{m}_2^0\right), \tag{19}$$

where $\hat{\mathbf{n}}$ denotes the normal of the diagonal wall as depicted in Fig. 16, is equivalent to $\tan\alpha = 2\hat{m}_2^0$. Therefore the piecewise-constant magnetization satisfying (19) mesoscopically carries no stray-field energy. Of course, on a microscopic scale Eq. (18) does not hold: The continuous transition in the wall generates a right-hand side, i.e., dipolar charges. Note that walls have to form since (18) does not allow for nontrivial smooth solutions with boundary data $\hat{m}_2 = 0$.

Within domain theory we therefore consider piecewise-constant magnetizations of concertina type of period $\hat{w}$ and of amplitude $\hat{m}_2 = \pm\hat{m}_2^0$ in the quadrangular and $\hat{m}_2 = 0$ in the triangular domains, such that (19) holds. Since the angles are fixed by (19), admissible configurations are characterized by two parameters, namely, the amplitude of the magnetization $\hat{m}_2^0$ and the width of the folds $\hat{w}$.

The energy which discriminates between these solutions is given by the total wall energy, which is an appropriate line-energy density integrated over the interfaces, augmented by Zeeman energy. We will see that the specific line energy is a function of the jump $[\hat{m}_2] = 2\hat{m}_2^0$ of the magnetization across the *vertical* wall—notice that the jump represents an infinitesimal version of the wall angle. Using the shear invariance of the reduced energy functional, namely,

$$\hat{x}_1 = s\hat{x}_2 + \tilde{x}_1, \quad \hat{x}_2 = \tilde{x}_2, \quad \hat{m}_2 = \tilde{m}_2 - s, \tag{20}$$

a diagonal wall can be transformed into a vertical wall for the choice of $s = \pm\frac{\hat{m}_2^0}{2}$. Hence it suffices to derive the specific line energy by restricting the reduced energy functional (exchange and stray-field energy) to one-dimensional (depending on $\hat{x}_1$ only) transitions with boundary data $\pm\hat{m}_2^0$ in the case of vertical walls and $\pm\frac{\hat{m}_2^0}{2}$ in the case of diagonal walls. The optimal transition layers are low-angle Néel walls whose line-energy density scales as

$$\hat{e}_{\text{wall}}\left(\frac{[\hat{m}_2]}{2}\right) = \hat{e}_{\text{wall}}\left(\hat{m}_2^0\right) \approx \frac{\pi}{8}\left(\hat{m}_2^0\right)^4 \ln^{-1}\frac{\hat{w}_{\text{tail}}}{\hat{w}_{\text{core}}}, \tag{21}$$

where $\hat{w}_{\text{tail}}$ and $\hat{w}_{\text{core}}$ are the two characteristic length scales of the Néel wall. The tails of the Néel wall decay only logarithmically and spread as much as possible. In the case of the concertina pattern, they are limited only by the neighboring walls—thus $\hat{w}_{\text{tail}} \approx \frac{\hat{w}}{4}$. A more careful inspection shows that the core width decreases with increasing jump size; more precisely, $\hat{w}_{\text{core}} \sim (\hat{m}_2^0)^{-2}$ (see Ref. 17, Sec. 3.5.5). Hence we obtain

$$\hat{e}_{\text{wall}}\left(\hat{m}_2^0\right) \approx \frac{\pi}{8}\left(\hat{m}_2^0\right)^4 \ln^{-1}\left[\hat{w}\left(\hat{m}_2^0\right)^2\right]. \tag{22}$$

The quartic dependence of the line energy with respect to $\hat{m}_2^0$ in Eqs. (21) and (22), respectively, is not surprising. It is known[5], Sec. 3.6.4] that the dominant energy contribution of the Néel wall comes from the stray-field energy generated by the charges in the logarithmically decaying tails. Since the stray-field energy is quadratic in the stray field and the stray field is quadratic itself in m_2 for a one-dimensional profile independent of x_2 [see (11)], the line energy (22) is to leading order quartic in m_2. The occurrence of *two* characteristic length scales and the logarithm in Eq. (21) are more subtle; see Refs. 18 and 11, Sec. 6.

Let us mention for completeness that, undoing the rescaling (12) and (13), we find that (22) turns into

$$e_{\text{wall}}\left(m_2^0\right) \approx \frac{\pi}{8}t^2\left(m_2^0\right)^4 \ln^{-1}\left[d^{-2}tw\left(m_2^0\right)^2\right]. \tag{23}$$

Within the class of admissible magnetizations, the domain-theoretical energy becomes a function of only three parameters, namely, $\hat{m}_2^0$, $\hat{w}$, and $\hat{h}_{\text{ext}}$. To see this, notice that one period of the pattern in Fig. 16 contains

(a) two vertical walls of length $1-\frac{\hat{w}}{\hat{m}_2^0}$ and of jump size $2\hat{m}_2^0$, leading to an energy contribution of $2\left(1-\frac{\hat{w}}{\hat{m}_2^0}\right)\hat{e}_{\text{wall}}(\hat{m}_2^0)$,

(b) four diagonal walls that can be shear-transformed to vertical walls of length $\frac{\hat{w}}{\hat{m}_2^0}$ and of jump size $\hat{m}_2^0$, leading to an energy contribution of $4\,\frac{\hat{w}}{\hat{m}_2^0}\,\hat{e}_{\text{wall}}(\frac{\hat{m}_2^0}{2})$, and

(c) two quadrangular domains of total area $\hat{w}-\frac{\hat{w}^2}{\hat{m}_2^0}$, leading to a Zeeman energy of $-\hat{h}_{\text{ext}}(\hat{m}_2^0)^2\left(\hat{w}-\frac{\hat{w}^2}{\hat{m}_2^0}\right)$.

The actual reason for considering the projected length in the case of diagonal walls is the anisotropic rescaling of the domain. Notice that the triangular domains do not contribute to the Zeeman energy since $\hat{m}_2 \equiv 0$ within these regions. Hence, the total domain energy per period in rescaled variables is given by

$$\hat{E}_{\text{domain}}\left(\hat{m}_2^0, \hat{h}_{\text{ext}}, \hat{w}\right) = 2\left(1 - \frac{\hat{w}}{\hat{m}_2^0}\right)\hat{e}_{\text{wall}}\left(\hat{m}_2^0\right) + 4\frac{\hat{w}}{\hat{m}_2^0}\,\hat{e}_{\text{wall}}\left(\frac{\hat{m}_2^0}{2}\right) - \hat{h}_{\text{ext}}\left(\hat{m}_2^0\right)^2\left(\hat{w} - \frac{\hat{w}^2}{\hat{m}_2^0}\right). \tag{24}$$

Within the original scaling the domain-theoretical energy takes the form of

$$E_{\text{domain}}\left(m_2^0, h_{\text{ext}}, w\right) = 2\left(\ell - \frac{w}{m_2^0}\right)e_{\text{wall}}\left(m_2^0\right) + 4\frac{w}{m_2^0}\,e_{\text{wall}}\left(\frac{m_2^0}{2}\right) - h_{\text{ext}}\left(m_2^0\right)^2 t\left(w\ell - \frac{w^2}{m_2^0}\right). \tag{25}$$

First of all we apply (24) in the next section to derive the optimal amplitude of the $\hat{w}^*$-periodic concertina pattern as a function of the external field $\hat{h}_{\text{ext}}$ by optimizing the energy in $\hat{m}_2^0$. Of course, domain theory is applicable and thus a good approximation only for the reduced model for $\hat{h}_{\text{ext}} \gg 1$, in which case there is a clear scale separation between walls and domains. Figure 17 shows that in this case domain theory is in good agreement with our numerical simulations of (15).

Before we go on with the analysis of domain theory let us emphasize that the experimentally observed concertina is of course not of uniform period and equal amplitude as is our domain-theoretical ansatz above. As shown in Fig. 18, there are also oblique piecewise-constant weak solutions of (18). Nevertheless this class of ansatz functions is very rigid: An elementary calculation shows that the location of the interior

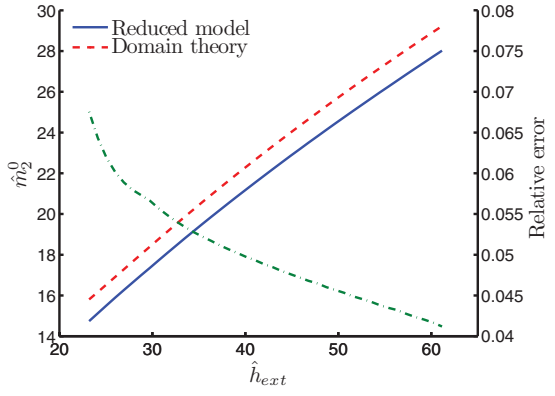

FIG. 17. (Color online) Domain theory and numerical simulations: The domain-theoretical prediction for the *rescaled* optimal amplitude (dashed) and the computed amplitude based on the reduced model (solid); corresponding values on the left axis. For the reduced model we display the amplitude, i.e., the maximal value which is attained in the quadrangular domain. The right axis indicates the value of the relative error (dot dashed).

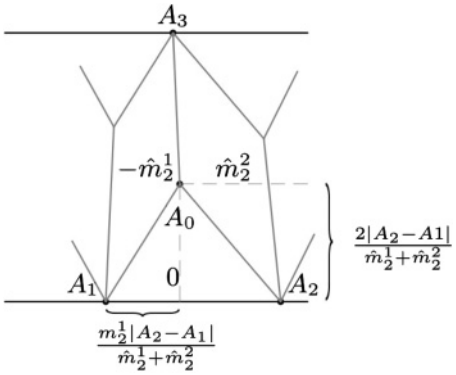

FIG. 18. Domain theory: Generalized tilted ansatz function.

triplet A_0 is uniquely determined by the jump condition (19), if the distances between the boundary triplets A_2 and A_1 and $\hat{m}_2^1$ and $\hat{m}_2^2$ on both sides are given. Hence the continuation of the pattern is uniquely determined if either the amplitude in the next quadrangular domain or the location of the next triplet, i.e., the width of the next quadrangular domain, is prescribed.

III. COARSENING OF THE CONCERTINA PATTERN

A. Domain theory: The optimal period of the concertina pattern for large external fields

Experiments show an increase in the average concertina period w as the external field h_{ext} is increased after the pattern has formed; see Fig. 2. The general tendency that the optimal period w is an increasing function of h_{ext} can be understood on the basis of domain theory in the reduced variables $\hat{m}_2^0$, $\hat{h}_{\text{ext}}$, and $\hat{w}$. By optimizing the energy per *unit length* with respect to the period $\hat{w}$ *and* the amplitude $\hat{m}_2^0$ of the transverse component, we obtain the following scaling of the optimal period of the pattern as a function of the external field:

$$\hat{w}_a(\hat{h}_{\text{ext}}) \sim \hat{h}_{\text{ext}} \ln \hat{h}_{\text{ext}}, \quad \hat{h}_{\text{ext}} \gg 1. \tag{26}$$

In particular we find that the optimal period increases with increasing field $\hat{h}_{\text{ext}}$—the a in w_a indicates absolute minimizer. Domain theory also yields the (same) scaling behavior for the optimal transverse component of the magnetization:

$$\hat{m}_{2a}(\hat{h}_{\text{ext}}) \sim \hat{h}_{\text{ext}} \ln \hat{h}_{\text{ext}}, \quad \hat{h}_{\text{ext}} \gg 1. \tag{27}$$

We note that both scalings have also been confirmed by a rigorous asymptotic analysis of the reduced energy functional (15) which does not rely on a simple concertina ansatz; cf. Theorem 1 in Ref. 19, p. 147. Moreover, numerical simulations of the reduced energy show that the optimal period increases with $\hat{h}_{\text{ext}}$ also for external fields close to the critical field; see Fig. 19. The optimal period shown in this diagram was computed by minimizing the energy per unit length with respect to both the magnetization and the period, for varying external field.

B. Coarsening: A modulation instability

Although the above analysis predicts that the optimal period $\hat{w}_a$ increases as the field $\hat{h}_{\text{ext}}$ increases, it does not explain why and in what way a concertina pattern of period $\hat{w}$ becomes *unstable* as $\hat{h}_{\text{ext}}$ increases. We will see that both the increasing

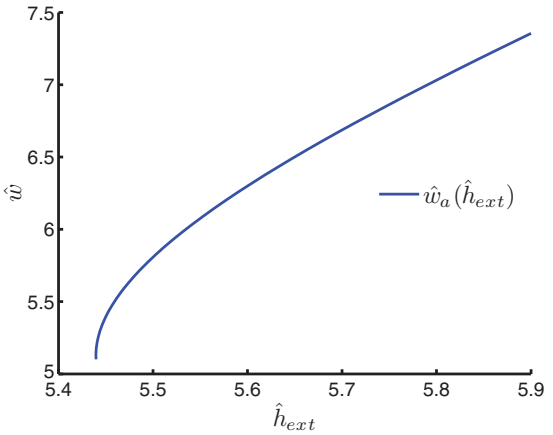

FIG. 19. (Color online) Numerical simulations: The optimal period of the concertina pattern as a function of the external field computed on the basis of the reduced model.

period for large fields and the deviation of the initial period close to the critical field from that of the unstable mode are due to an instability under long-wavelength modulations of the pattern. The mechanism behind the instability is the following: Given $\hat{h}_{\text{ext}}$ and a period $\hat{w}$, an optimization in the transverse component $\hat{m}_2$ yields the result that the optimal energy *per period* $\hat{E}_{\text{opt}}(\hat{h}_{\text{ext}},\hat{w})$ is a concave function of $\hat{w}$ if $\hat{h}_{\text{ext}}$ is sufficiently large. The concavity suggests—as depicted in Fig. 20—that the concertina pattern of a uniform period $\hat{w}$ becomes unstable toward perturbations which increase the period to $\hat{w}+\epsilon$ and the corresponding amplitude of the transverse component to $\hat{m}_2^0(\hat{w}+\epsilon)$ in some folds, and decrease the period to $\hat{w}-\epsilon$ and the amplitude to $\hat{m}_2^0(\hat{w}-\epsilon)$ in other folds. This modulation eventually leads to the collapse of the smaller folds, i.e., coarsening. However, in view of the nonlocal character of the stray-field energy, it is not clear whether this simplified picture, i.e., that the energy of the modulation amounts to the modulation of the energy, applies. As we shall see in Sec. III C, a modulation of the period on a very long length scale overcomes this objection. Thus the concavity of the minimal energy implies an instability under long-wavelength modulations of the pattern.

In order to derive the concavity of the minimal energy, we apply domain theory for large external fields in Sec. III C and

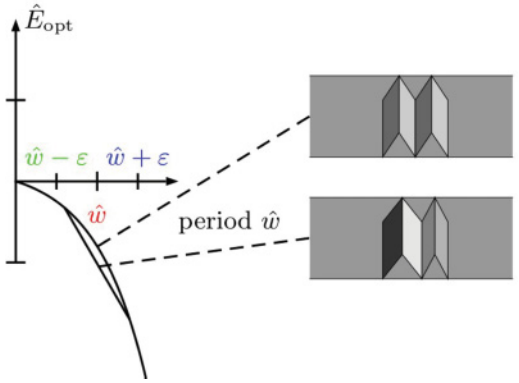

FIG. 20. (Color online) Concavity of the minimal energy per period implies an instability under modulation of the wavelength.

an extended bifurcation analysis close to the critical field in Sec. III D. We will see that both asymptotics match the results of the numerical simulation of our reduced model.

Let us mention that the modulation instability of the concertina pattern is closely related to the so-called Eckhaus instability, which was discovered in the context of nonlinear instabilities in convective systems leading to a change in wavelength of the observed periodic pattern; cf. Ref. 20.

C. Bloch-wave theory: Instability with increasing field

As indicated above, not only the optimal period but also the coarsening can be explained on the basis of domain theory for large external fields $\hat{h}_{\text{ext}} \gg 1$. This relies on the optimal energy per period $\min_{\hat{m}_2} \hat{E}_{\text{domain}}(\hat{m}_2,\hat{h}_{\text{ext}},\hat{w})$. For periods $\hat{w}$ much smaller than the optimal period at some value of the external field $\hat{h}_{\text{ext}}$, i.e., $\hat{w} \ll \hat{h}_{\text{ext}} \ln \hat{h}_{\text{ext}}$, we find that

$$\min_{\hat{m}_2} \hat{E}_{\text{domain}}(\hat{m}_2,\hat{h}_{\text{ext}},\hat{w}) \sim -\hat{h}_{\text{ext}}^2 \hat{w}^2 \ln(\hat{h}_{\text{ext}}\hat{w}^2). \qquad (28)$$

In particular, the optimal energy per period in Eq. (28) is *concave* in the period $\hat{w}$. Although domain theory therefore suggests an instability under wavelength modulation for periods which are much smaller than the optimal period, it is too rigid to allow for such a type of perturbation, even in the class of generalized ansatz functions; cf. Fig. 18.

It is rather on the level of the reduced model that it can be seen that the concavity translates into an instability (despite the potentially long-range interactions via the stray field). Indeed, a Bloch-wave analysis of the reduced model shows that the concavity is in a one-to-one correspondence with an instability under long-wavelength modulations of the pattern. In the Bloch-wave analysis one considers $N\hat{w}$-periodic eigenfunctions of the Hessian of the form $\delta\hat{m}_2 = e^{-i\hat{x}_1\hat{k}_1}\,\delta\hat{m}_2^{\hat{k}_1}$ with wave number $\hat{k}_1 = \frac{2\pi}{N\hat{w}}$ and N some large integer, and where $\delta\hat{m}_2^{\hat{k}_1}$ is $\hat{w}$-periodic with respect to $\hat{x}_1$, i.e., one considers sinusoidal modulations of some suitable $\hat{w}$-periodic function. An asymptotic expansion of

$$\text{Hess}\,\hat{E}_0(\hat{m}_2)\big(e^{-i\hat{x}_1\hat{k}_1}\delta\hat{m}_2^{\hat{k}_1}\big) = \lambda^{\hat{k}_1} e^{-i\hat{x}_1\hat{k}_1}\,\delta\hat{m}_2^{\hat{k}_1} \qquad (29)$$

for small wave numbers $\hat{k}_1 \ll 1$, i.e., $N \gg 1$, shows that the first eigenvalue can be related to the second derivative of the optimal energy per period $\hat{E}_{\text{opt}} = \min_{\hat{m}_2} \hat{E}$. More precisely, one can show that the eigenvalue possesses the expansion

$$\lambda^{\hat{k}_1} \approx c_0\, \hat{k}_1^2 \frac{d^2}{d\hat{w}^2} \hat{E}_{\text{opt}}(\hat{h}_{\text{ext}},\hat{w}) \quad \text{for} \quad \hat{k}_1 \ll 1,$$

where c_0 denotes a constant that depends on $\hat{m}_2$; see Ref. 21, Theorem 5.1. This rigorously shows that the concavity of $\hat{E}_{\text{opt}}(\hat{h}_{\text{ext}},\hat{w})$ with respect to the period $\hat{w}$ implies that the concertina pattern of a given period $\hat{w}$ is unstable. Domain theory predicts that the marginally stable period $\hat{w}_s$, i.e., $\hat{w}_s$ such that $\frac{d^2}{d\hat{w}^2}\hat{E}_{\text{opt}}(\hat{h}_{\text{ext}},\hat{w}_s) = 0$, scales as $\hat{w}_s \sim \hat{h}_{\text{ext}} \ln \hat{h}_{\text{ext}}$ [cf. (28)]—we note that the s in w_s stands for marginally stable. Figure 21 displays the optimal and the marginally stable periods computed on the basis of the reduced energy functional. Figure 22 shows that the computation of the optimal and the marginally stable periods on the basis of domain theory matches the numerical simulations on the basis of the reduced model.

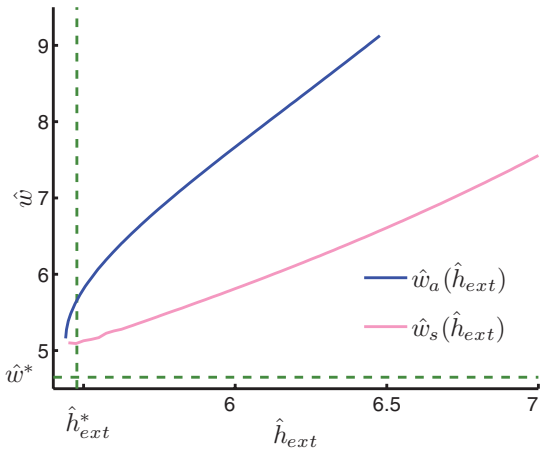

FIG. 21. (Color online) Numerical simulations: Comparison of the optimal and marginally stable periods of the concertina pattern as a function of the external field, both computed on the basis of the reduced model. In the region below the red (lower) curve the minimal energy per period is concave and thus a concertina of that period is unstable and coarsens.

D. Bifurcation analysis: Instability for small fields

The numerical computations (see Fig. 21) show that the optimal energy per period is concave not only for large external fields as predicted by domain theory. In fact, we extract from our numerical data that $\frac{d^2}{d\hat{w}^2}\hat{E}_{\rm opt}(\hat{h}_{\rm ext},\hat{w}^*)$ is negative also for small external fields up to the turning point. This is consistent with the numerical computation of the eigenvalue λ^N based on the asymptotic expansion of Eq. (29). Hence, the Bloch-wave analysis implies that the $\hat{w}^*$-periodic concertina pattern is unstable under long-wavelength modulations close to the critical field.

This qualitatively explains the trend in the deviation of the initial concertina period $w^*_{\rm expt}$ from the period of the unstable mode; see Sec. I G. Close to the critical field, the concavity can be confirmed with the help of an asymptotic bifurcation analysis. To see this, we extend our ansatz from

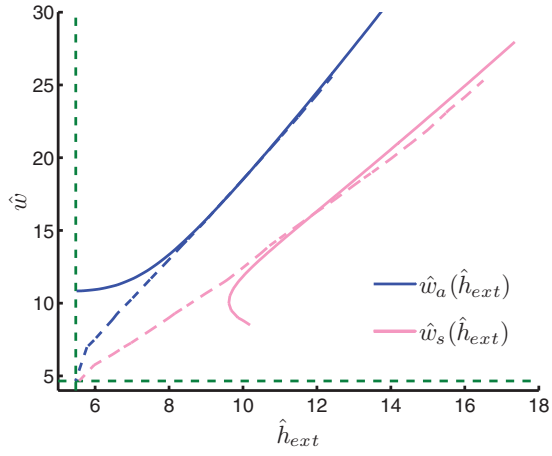

FIG. 22. (Color online) Numerical simulations and domain theory: The optimal and marginally stable periods computed on the basis of the reduced model (dashed) match the predictions on the basis of domain theory in the regime $\hat{h}_{\rm ext} \gg 1$.

Sec. II and take into account small deviations of the wave number, $\hat{k} = \hat{k}^* + \delta\hat{k}$. As we have seen in Eq. (17) in Sec. II, the quartic coefficient in the energy expansion, namely, $\frac{\pi}{640}$, is small compared to the second-order coefficient and the scale of the reduced external field. Due to that degeneracy it is necessary to additionally take into account a contribution of cubic order in the perturbation of $\hat{m}_2 = 0$, i.e., we use the extended ansatz

$$\hat{m}_2 \approx A\hat{m}_2^* + A^2\hat{m}_2^{**} + A^3\hat{m}_2^{***}.$$

Optimization of the coefficients in the expansion of the energy with respect to A subsequently in $\hat{m}_2^{**}$ and $\hat{m}_2^{***}$ leads to an expansion of the energy density of the form

$$\frac{\hat{k}}{2\pi}\hat{E}_0(A\hat{m}_2^* + A^2\hat{m}_2^{**} + A^3\hat{m}_2^{***}) \approx \frac{1}{4}[\hat{h}^*_{\rm ext}(\hat{k}) - \hat{h}_{\rm ext}]A^2 - c_4(\hat{k})A^4 + c_6(\hat{k})A^6,$$

where $c_4(\hat{k}^*) = \frac{\pi}{640}\frac{\hat{k}^*}{2\pi}$ in accordance with (17). Hence, under the assumption that $c_4(\hat{k}^*) \approx 0.001\,05$ is small, the energy density to leading order can be approximated by

$$\frac{\hat{k}}{2\pi}\hat{E}_0(A\hat{m}_2^* + A^2\hat{m}_2^{**} + A^3\hat{m}_2^{***}) \approx \frac{1}{4}\left(\frac{d^2}{d\hat{k}^2}\hat{h}^*_{\rm ext}(\hat{k})_{|\hat{k}=\hat{k}^*}\frac{\delta\hat{k}^2}{2} + \delta\hat{h}_{\rm ext}\right)A^2 - \left(c_4(\hat{k}^*) + \frac{d}{d\hat{k}}c_4(\hat{k})_{|\hat{k}=\hat{k}^*}\delta\hat{k}\right)A^4 + c_6(\hat{k}^*)A^6. \quad (30)$$

The numerical values of the coefficients are given by

$$\frac{d^2}{d\hat{k}^2}\hat{h}^*_{\rm ext}(\hat{k})_{|\hat{k}=\hat{k}^*} = 3, \quad \frac{d}{d\hat{k}}c_4(\hat{k})_{|\hat{k}=\hat{k}^*} \approx -0.0217, \quad c_6(\hat{k}^*) \approx 0.000\,207.$$

Notice that $c_6(\hat{k}^*)$ is positive, confirming the numerically observed turning point of the $\hat{w}^*$-periodic branch. Obviously, the asymptotic expansion displays an asymmetric behavior in $\delta\hat{k}$; the energy decreases for $\delta\hat{k} < 0$. Based on the expansion (30), one can characterize the optimal wave number and the optimal period. We note that the concavity of the minimal energy per period as a function of the period is equivalent to the concavity of the energy density as a function of the wave number $\hat{k}$:

$$\frac{d^2}{d\hat{w}^2}\hat{E}_0(\hat{w}) = \frac{\hat{k}^3}{(2\pi)^2}\frac{d^2}{d\hat{k}^2}\left[\hat{k}\hat{E}_0\left(\frac{2\pi}{\hat{k}}\right)\right].$$

Figure 23 shows the optimal period and the marginally stable period calculated on the basis of (30). We read off that the $\hat{w}^*$-periodic concertina pattern is indeed unstable at the critical field.

A comparison between Figs. 21 and 23 shows that the predictions on the basis of the asymptotic expansion differ from the optimal and the marginally stable periods computed on the basis of the reduced model; compare for example the scale of the external field. This deviation is related to our assumption that the quartic coefficient is small so that the energy can be approximated by (30). On the other hand, Fig. 24 shows that the asymptotics match the reduced model if we add a quartic contribution $+\frac{\hat{Q}}{4}\int m_2^4$ to the reduced energy, where

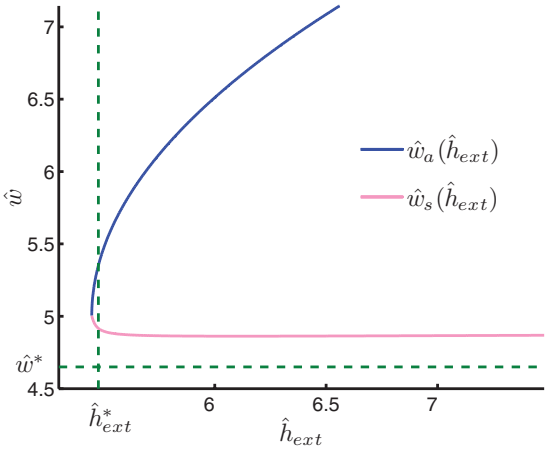

FIG. 23. (Color online) Bifurcation analysis: The optimal and marginally stable periods as functions of the external field obtained on the basis of the extended bifurcation analysis.

the value of the parameter $\hat{Q}$ is such that the contribution cancels $c_4(\hat{k}^*)$ in Eq. (30) (which happens for $\hat{Q} \approx 0.03$). We will see later that such an additional quartic contribution has a physical meaning if we take into account a uniaxial anisotropy; see Sec. VI. It turns out that $\hat{Q}$ is an appropriately rescaled quality factor Q.

E. Numerical bifurcation analysis: Type of secondary instability and downhill path in energy landscape

With the help of a bifurcation-detection algorithm we are able to compute the field at which the $\hat{w}^*$-periodic concertina becomes unstable under $N\hat{w}^*$-periodic perturbations while we follow the primary branch. Figure 25 shows the secondary critical fields; as expected (see Sec. III D and Fig. 21) the secondary instability approaches the turning point as the integer N increases. We note that the secondary instability is reached for finite N.

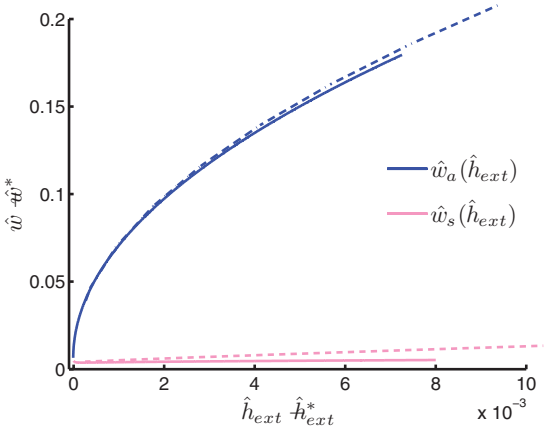

FIG. 24. (Color online) Numerical simulations and bifurcation analysis: The prediction on the basis of the reduced model (dashed) matches the prediction on the basis of the extended bifurcation analysis for a near-degenerate value of $\hat{Q} = 0.0295$ close to $\hat{Q}^* \approx 0.03$; cf. Sec. VI.

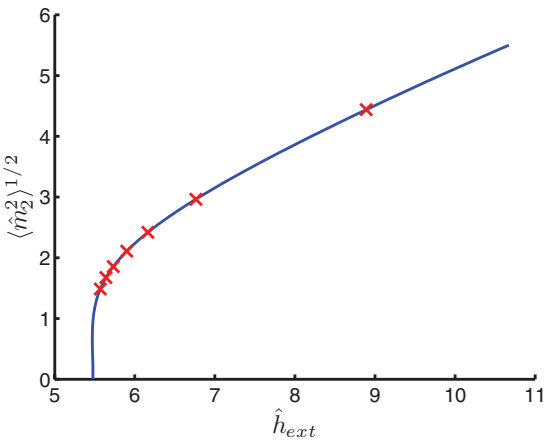

FIG. 25. (Color online) Numerical simulations: The appearance of the secondary instability under $N\hat{w}^*$-periodic perturbations as a function of N; the markers indicate the occurrence of the instability for $N = 2, \ldots, 8$ (right to left). The critical field for $N = 8$ is 5.602.

In the following we want to study the *way* in which the concertina pattern becomes unstable. We first present the outcome of the computation of the secondary bifurcation branches; Fig. 26 shows part of the bifurcation diagram. We point out that, due to the symmetries of the pattern, the bifurcations are not simple in the sense that more than one branch bifurcates.

The symmetries of the pattern can be identified as linear representations of the dihedral group D_{2N}, where N indicates the number of folds. The secondary bifurcation branches are computed with the help of a numerical branch-switching algorithm which is adapted to the problem of multiple bifurcations. Generically, there are two distinct types of branch: branches along which rotational symmetry is broken and reflectional symmetry is conserved and vice versa (see Fig. 27). In the case of the first type of branch, a fold collapses as two neighboring faces disappear; in the case of the second type of branch, the number of folds decreases as one face disappears and the two adjacent faces merge. During the coarsening process, the width

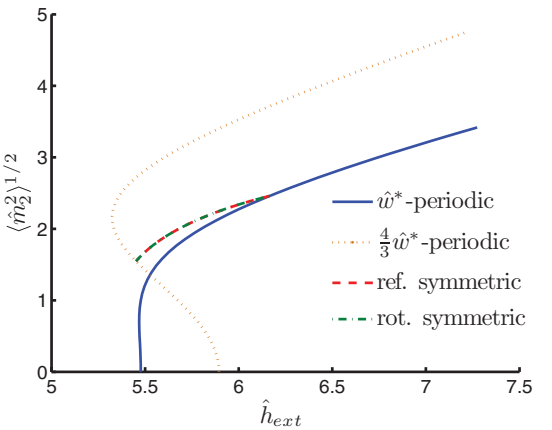

FIG. 26. (Color online) Numerical simulations. Bifurcation diagram for $4\hat{w}^*$ perturbations: The bifurcation branches that connect the $\hat{w}^*$-periodic (blue solid) and the $\frac{4}{3}\hat{w}^*$-periodic (orange dashed) branches. The magnetization patterns at the indicated fields are shown in Fig. 27.

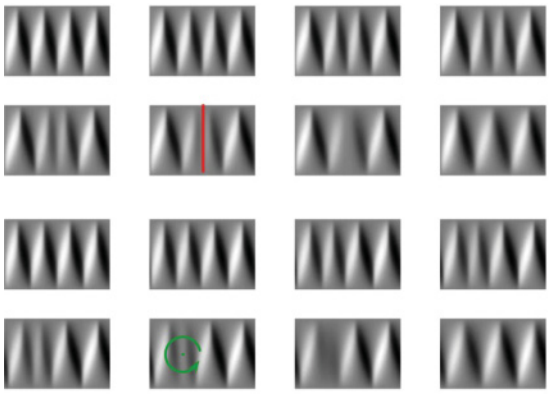

FIG. 27. (Color online) Numerical simulations: Reflectional-symmetric with respect to center wall (top two rows) and rotational-symmetric with respect to the midpoint of the white face (bottom two rows) magnetization patterns on the unstable bifurcation branch connecting the $\hat{w}^*$-periodic and the $\frac{4}{3}\hat{w}^*$-periodic branches. The central fold collapses (top); the white face disappears and two adjacent black faces merge (bottom). The computational domain is $\hat{\Omega} = [0,4\hat{w}) \times [0,1]$.

of the remaining folds is adjusted. Let us point out that the first instability of the $\hat{w}$-periodic concertina under $N\hat{w}$-periodic perturbations in the end leads to the collapse of exactly one fold, reducing the total number of folds from N to $N-1$; see Fig. 25.

F. Wavelength modulation in the experiments

In the experiments, the x_1 wavelength of the modulation is restricted by the finite sample size. Moreover, inhomogeneities and defects of the material, in particular those at the edges of the cross section, strongly affect the formation of the pattern. This is reflected by the fact that walls occur at the same pinning sites when the experiment is rerun. The existence of pinning sites hence leads to an effective modulation wavelength that is just a small multiple N of the wavelength of the pattern. In particular we expect that pinning sites have a stabilizing effect and therefore prevent coarsening. Therefore, the seemingly artificial numerical simulation for small and moderate N (cf. Fig. 25) may be more relevant for the experiment than the Bloch-wave analysis, i.e., $N \nearrow \infty$ (cf. Sec. III C).

G. Domain theory: Instability for decreasing field

The experiments also show that the concertina period $\hat{w}$ decreases with *decreasing* external field $\hat{h}_{\text{ext}}$. This has a simple explanation on the level of domain theory, too. Suppose that the concertina period had increased at several coarsening events during the increase of the field. As the decreasing external field $\hat{h}_{\text{ext}}$ drops below its optimal scaling given the period $\hat{w}$, that is, for $\hat{w} \gg \hat{h}_{\text{ext}} \ln \hat{h}_{\text{ext}}$, the optimal concertina pattern does not suffer a long-wavelength instability, but instead degenerates in the sense that the closure domains invade the whole cross section. Simulations of the reduced model confirm this scenario predicted by domain theory; see Fig. 28, which shows a pattern of period $5\hat{w}^*$ close to the turning point: The numerical backward cycle, in which we start at the multiply coarsened state and then after minimization

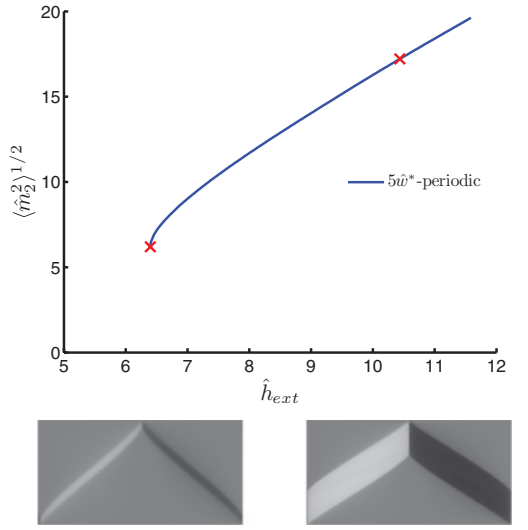

FIG. 28. (Color online) Numerical simulations: The coarsened concertina pattern degenerates as the external field is reduced. The numerical simulations confirm the prediction based on domain theory: The pattern degenerates at the turning point of the branch. The computational domain is $\hat{\Omega} = [0,5\hat{w}) \times [0,1]$.

repeatedly decrease the external field by a fixed increment, shows that the coarsened pattern stays stable up to the turning point that coincides with the moment at which the pattern degenerates as mentioned above. Depending on the initial level of coarsening, either the period is then reduced or we reach the uniformly magnetized state after the minimization.

H. Conclusion: Hysteresis and scattering of data

Summing up, domain theory in conjunction with a Bloch-wave argument indicates that the concertina pattern of period w is present or stable at a given field h_{ext} if and only if $w \sim \ell^2 t^{-1} h_{\text{ext}} \ln(d^{-2/3} \ell^{4/3} t^{-2/3} h_{\text{ext}})$, which is confirmed by the numerical simulations. In particular we expect that the height of the triangular domains ($\sim \frac{w}{m_2^0}$) is close to constant as the external field increases; cf. (26) and (27). If the period deviates by a (large) factor from that expression, it becomes unstable. On the other hand, this analysis also suggest that there is a *range* of $w \sim \ell^2 t^{-1} h_{\text{ext}} \ln d^{-2/3} \ell^{4/3} t^{-2/3} h_{\text{ext}}$ for which the concertina pattern is stable; see Fig. 29. This may explain some of the scatter in the experimental data and the pattern's hysteresis.

Figure 29 displays the marginally stable period [below the red (lowest) curve the minimal energy per period is concave and thus the concertina of smaller period unstable as the field increases] and the optimal period depending on the external field. The top green curve indicates the turning points of the $\hat{w}_m$-periodic branches, i.e., the smallest external field for which a concertina of a certain maximal period $\hat{w}_m$ exists—the m in $\hat{w}_m$ indicates maximal. Observe that the maximal period $\hat{w}_m$ on the basis of domain theory and on the basis of the reduced model coincide for large external field, too. The region bounded by $\hat{w}_s$ and $\hat{w}_m$ corresponds to the range of stable periods. Figure 30 displays an expected hysteresis loop deduced from numerical simulations. Figure 31 shows a real hysteresis loop as experimentally observed.

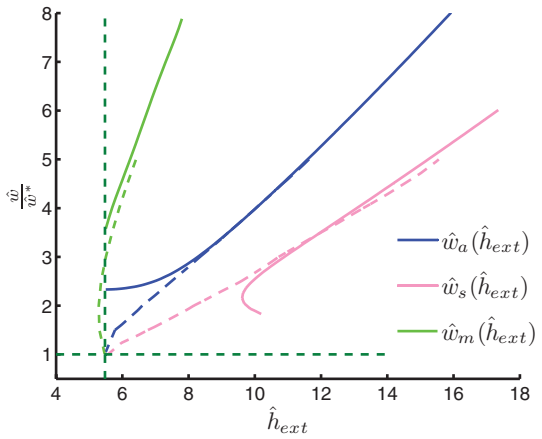

FIG. 29. (Color online) Numerical simulations: The marginally stable (bottom curves), optimal (middle curves), and maximal period (top curves) of the concertina pattern as functions of the external field $\hat{h}_{\text{ext}}$. The dashed and solid curves depict the results on the basis of the reduced model and on the basis of domain theory, respectively.

IV. DISCRETIZATION AND NUMERICAL SIMULATIONS

The numerical simulations are based on a finite-difference discretization of the reduced rescaled energy functional (15). The transverse component $\hat{m}_2$ is approximated on a uniform Cartesian grid. The discretization of the exchange, anisotropy and Zeeman energy is straightforward. In the case of nonlinear charge density $\hat{\sigma} = -\hat{\partial}_1 \frac{\hat{m}_2^2}{2} + \hat{\partial}_2 \hat{m}_2$ our choice of a finite-difference stencil is motivated by the inheritance of the shear invariance (20). The stray-field energy can efficiently be computed using fast Fourier transform with respect to $\hat{x}_1$. For an introduction to the discretization scheme, see Ref. 17, Sec. 3.2. Note that the computation of the energy and related quantities, such as the gradient or Hessian, can be parallelized since the nonlocality is only with respect to one dimension. For the parallelization we decompose the computational domain into horizontal slices with respect to $\hat{x}_2$.

We apply numerical simulations to compute (local) minimizers and stationary points. The naive approach using steepest-descent algorithms for the computation of minimizers is slow and even fails close to bifurcation points. The iterative path-following techniques that we apply in order to compute an approximation to a branch of stationary points are adapted to such situations; cf. Ref. 22. The local tangent t^n at a stationary point $(\hat{\mathbf{m}}^n, \hat{h}^n_{\text{ext}})$ of the branch is used to obtain a predictor for the next point on the branch $(m_2^{n+1}, h_{\text{ext}}^{n+1})$; see Fig. 32. Within the corrector step the predictor is orthogonally (to the tangent) projected onto the branch. This step amounts to the solution of a nonlinear equation, more precisely an augmented Euler-Lagrange equation:

$$\begin{pmatrix} \nabla_{\hat{m}_2} \hat{E}_0(\hat{\mathbf{m}}_2^{n+1}, \hat{h}_{\text{ext}}^{n+1}) \\ \left[(\hat{\mathbf{m}}_2^{n+1}, \hat{h}_{\text{ext}}^{n+1}) - p^{n+t}\right] \cdot t^n \end{pmatrix} = 0.$$

A bifurcation point can be detected with the help of an appropriate indicator function; cf. Ref. 22. However, both the bifurcation detection and the branch-switching technique which are described in that reference are applicable for simple bifurcations points only. As described in detail in Ref. 21, both methods can be modified in order to cope with multiple bifurcation points. This extension relies on the fact that multiple bifurcations which occur due to symmetries of the primary solution generically can be reduced to simple bifurcation points; cf. Ref. 23.

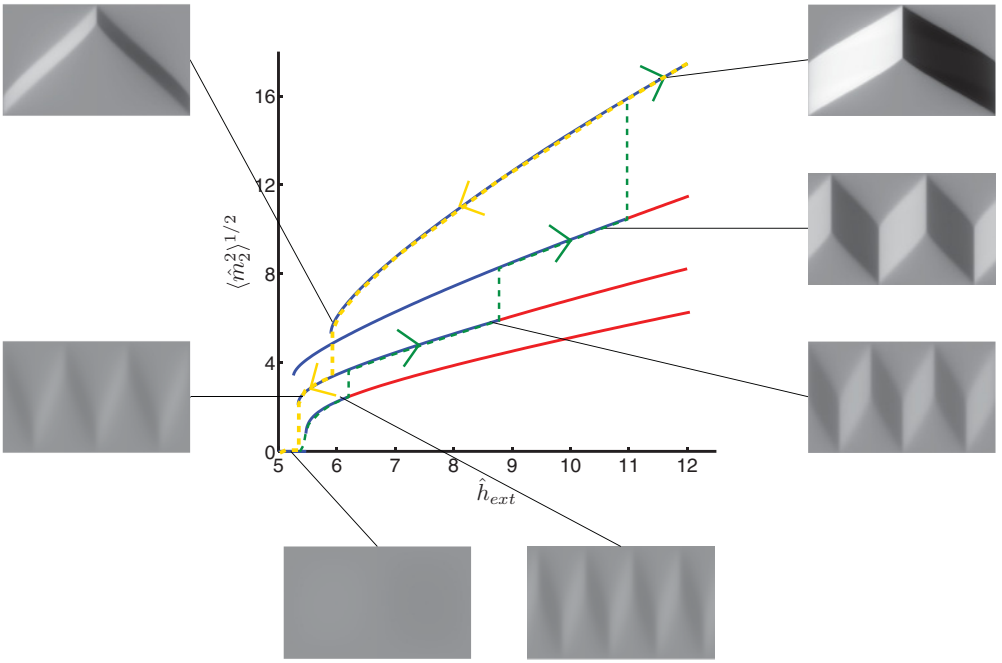

FIG. 30. (Color online) Numerical simulations: The hysteresis loop. As we increase the field, the concertina pattern coarsens if the period is smaller than the stable period. As we decrease the field starting from a coarsened concertina the pattern degenerates as we reach the turning point of the branch. The pattern refines toward the optimal period until it finally disappears. The computational domain is $\hat{\Omega} = [0, 4\hat{w}) \times [0, 1]$.

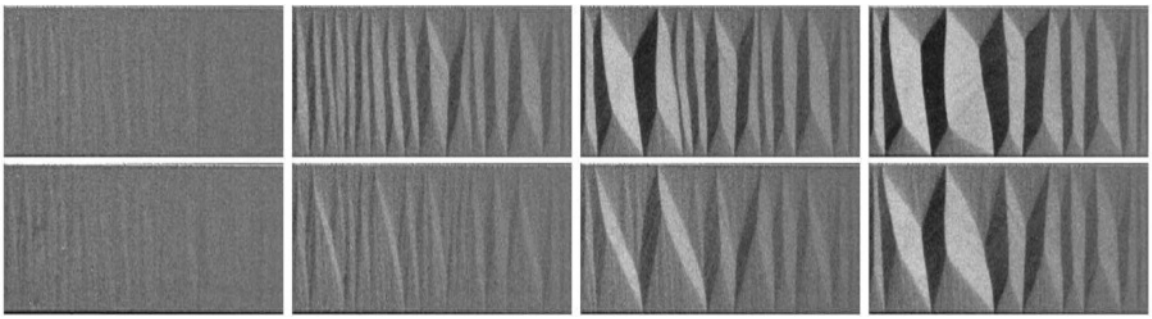

FIG. 31. Experiment: The hysteresis cycles of a Permalloy sample of 30 nm thickness and 50 μm width. The upper row shows the pattern as the external field increases (from left to right); the lower row shows the pattern as the external field decreases (from right to left).

V. POLYCRYSTALLINE ANISOTROPY

The experiments usually do not show a clear-cut critical field with a first-order transition (i.e., subcritical bifurcation). This can be due to lack of sensitivity (the amplitude of the transverse component $\langle m_2^2\rangle^{1/2} = d^{2/3}\ell^{-1/3}t^{-1/3}\langle \hat{m}_2^2\rangle^{1/2}$ at the turning point ranges between 0.015 and 0.063 for typical sample dimensions, namely, widths ℓ between 10 and 50 μm and thicknesses t between 30 and 100 nm) or the presence of the so-called ripples that smooth out the transition, as we shall explain in this section. A ripple is an in-plane small-scale oscillation of the magnetization—perpendicular to its average direction—in extended films. In this section, we show how the linear ripple theory developed in Refs. 24 and 25 can be incorporated into our theory for the concertina and explains the smoothing out of the first-order transition encountered in Sec. II.

The ripple is triggered by an effective field of random direction on a small scale. Several origins for this effective field have been proposed in the literature (see, for instance, Ref. 25, Sec. C); in polycrystalline thin films, the random orientation of the grains (via crystalline anisotropy) and local stresses (via magnetostriction) are seen as the main causes. In our discussion, we focus on the former.

Hoffmann[24] and Harte,[25] basing their work on the torque equilibrium, linearized around a spatially constant magnetization (solely determined by the external field and anisotropy). Hereby they identified the linear response to (for instance) such a small-scale, small-amplitude random effective field. The main finding is that the stray field—which penalizes transverse more than longitudinal perturbations of the magnetization because the former lead to a stronger charge oscillation—results in a strong anisotropy of the response.

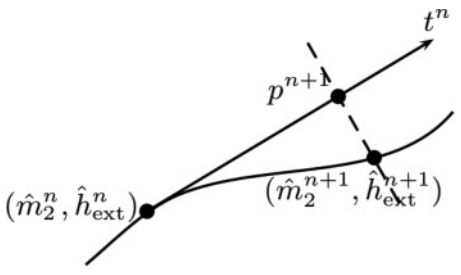

FIG. 32. Tangent predictor-corrector continuation method.

Clearly, the anisotropic rescaling (12) leading to our reduced model and the anisotropic response have the same origin. We will see that both the ripple and the transition between ripple and concertina can be explained within the framework of an extension of our reduced model. We note that our analysis of the ripple is mainly a reformulation of the classical results. However, the added insight is that the finite width ℓ of the sample leads to a (continuous) transition from the ripple to the concertina.

We now explain how to extend our reduced model. We start from the three-dimensional model (1) with a uniaxial anisotropy of strength Q and position-dependent easy axis $e(x)$, i.e., with the term $-Q\int(me)^2dx$. In the approximation of our reduced model, i.e., $m_3 \equiv 0$, $\mathbf{m} = m(x_1,x_2)$, and the linearization $m_1 \approx 1 - \frac{m_2^2}{2}$ due to $m_2^2 \ll 1$, this term is, up to additive constants, to leading order approximated by $-2Qt\int m_2\overline{e_1e_2}dx_1dx_2$, where $\overline{e_1e_2}(x_1,x_2)$ denotes the vertical average of the product of the first two components of the easy axis $e = (e_1,e_2,e_3)$. A random anisotropy therefore acts to leading order as a random transverse external field

$$-2t\int_{\Omega'} h_{\text{ripple}}m_2dx_1dx_2, \tag{31}$$

where $h_{\text{ripple}} = Q\overline{e_1e_2}$. As mentioned, the position dependence of e arises from the random orientation of the grains of size ℓ_{grain}. Provided $t \ll \ell_{\text{grain}} \ll w^*$ (where we take w^* as a typical length scale of the magnetization pattern), the stationary statistics of $\overline{e_1e_2}$ are characterized by

$$\langle \overline{e_1e_2}(0,0)\overline{e_1e_2}(x_1,x_2)\rangle = \ell_{\text{grain}}^2\delta(x_1)\delta(x_2)\langle \overline{e_1e_2}(0,0)^2\rangle, \tag{32}$$

where $\langle\cdot\rangle$ denotes the ensemble average and δ the Dirac function.

For subcritical fields $h_{\text{ext}} < h_{\text{ext}}^*$, we neglect the nonlinear term in the stray-field energy in Eq. (8). The resulting energy functional is quadratic and linear in m_2; hence it is conveniently expressed in terms of $\mathcal{F}m_2(k_1,k_2)$, which denotes the Fourier transform of m_2 in x_1, and the Fourier sine series in x_2:

$$E(m_2) \approx \int_{-\infty}^{\infty}\sum_{k_2\in\pi\mathbb{Z}/\ell}\left(d^2k_1^2 + \frac{1}{2}tk_2^2k_1^{-1} - h_{\text{ext}}\right)|\mathcal{F}m_2|^2 - 2\mathcal{F}h_{\text{ripple}}\mathcal{F}^{-1}m_2dk_1.$$

Explicit minimization yields

$$\mathcal{F}m_2(k_1,k_2) = \frac{1}{\left(d^2k_1^2 + \frac{1}{2}tk_2^2k_1^{-1} - h_{\text{ext}}\right)}\mathcal{F}h_{\text{ripple}}(k_1,k_2). \tag{33}$$

We interpret this m_2 as the ripple. Since (32) on the level of $\mathcal{F}\,\overline{e_1e_2}$ reads $\langle|\mathcal{F}\,\overline{e_1e_2}(k_1,k_2)|^2\rangle = \ell_{\text{grain}}^2$, (33) is best expressed in terms of the energy spectrum:

$$\langle|\mathcal{F}m_2(k_1,k_2)|^2\rangle = Q^2\frac{\ell_{\text{grain}}^2}{\left(d^2k_1^2 + \frac{1}{2}tk_2^2k_1^{-1} - h_{\text{ext}}\right)^2}. \tag{34}$$

This formula clearly displays the aforementioned anisotropic response of m_2 to the isotropic field h_{ripple}.

From formula (34) one can infer the predominant wave number of the ripple, that is,

$$\langle|k_1|\rangle = \frac{\sum_{k_2}\int_{-\infty}^{\infty}|k_1|\langle|\mathcal{F}m_2|^2\rangle dk_1}{\sum_{k_2}\int_{-\infty}^{\infty}\langle|\mathcal{F}m_2|^2\rangle dk_1}. \tag{35}$$

For moderate stabilizing fields $t^2d^{-2} \gg -h_{\text{ext}} \gg d^{-2/3}\ell^{4/3}t^{-2/3}$, we obtain from (35) that the average wave number scales as $\langle|k_1|\rangle \sim (-h_{\text{ext}})^{1/2}d^{-1} \ll td^{-2}$. This is the scaling of the predominant wave number of the ripple in an extended film [Ref. 24, p. 34, (7)]. Notice that the lower bound characterizing regime III is equivalent to $t^2d^{-2} \gg d^{-2/3}\ell^{4/3}t^{-2/3}$. For large stabilizing fields $-h_{\text{ext}} \gg t^2d^{-2}$ one can show that the average amplitude of the ripple, given by $\int\sum_{k_2}\langle|\mathcal{F}m_2|^2\rangle dk_1$, tends to zero. Moreover, from (35), because of the discreteness of k_2, we can infer

$$\lim_{h_{\text{ext}}\uparrow h_{\text{ext}}^*}\langle|k_1|\rangle = \frac{2\pi}{w^*},$$

which is the wave number of the unstable mode (7). We thus learn that, as the strength h_{ext} of the external field increases from negative values toward the critical value, the average wavelength of the ripple continuously increases from the values characteristic for a film which is infinite in both the x_1 and x_2 directions to the wavelength of the unstable mode that is at the origin of the concertina pattern (which depends on the sample width). Due to this transition it is thus not surprising that the ripple and the small-amplitude concertina are difficult to distinguish.

We now address the numerical simulation of our augmented model (36). Let us therefore first rewrite the additional term (31) in the rescaled variables (12). The rescaled reduced model (15) is augmented by

$$-2\int\hat{h}_{\text{ripple}}\hat{m}_2 d\hat{x}_1 d\hat{x}_2, \tag{36}$$

where $\hat{h}_{\text{ripple}}$ is a stationary Gaussian field of vanishing mean and of variance

$$\langle\hat{h}_{\text{ripple}}(0,0)\hat{h}_{\text{ripple}}(\hat{x}_1,\hat{x}_2)\rangle = (\sigma^*)^2\delta(\hat{x}_1)\delta(\hat{x}_2), \tag{37}$$

with $\sigma^* = d^{-10/6}\ell^{5/6}t^{-1/6}Q\ell_{\text{grain}}\langle\overline{e_1e_2}(0,0)^2\rangle^{1/2}$. In the case of a uniform distribution of the anisotropy axis in the plane, we have for example that $\langle\overline{e_1e_2}(0,0)^2\rangle = \frac{1}{8}$.

On the level of the discretization, the field $\hat{h}_{\text{ripple}}$ is modeled as a Gaussian random variable of mean zero, which is identically and independently distributed from grid point to grid point and has variance $(\sigma^*)^2{\Delta\hat{x}_1}^{-1}{\Delta\hat{x}_2}^{-1}$, where $\Delta\hat{x}_i$ denotes the grid size in direction $\hat{x}_i$. For the numerical simulations we thus have to determine the value of σ^* for a typical sample. Let us consider a film of 30 nm thickness and 70 μm width with typical grain size $\ell_{\text{grain}} = 15$ nm. For a local strength of anisotropy $Q = 5\times10^{-3}$ we obtain that $(\sigma^*)^2 = 125.87$. For the value of $(\sigma^*)^2 = 110.83$, our numerical simulation indeed shows a continuous transition from the ripple to the concertina pattern instead of a first-order phase transition due to a subcritical bifurcation; see Fig. 33.

We also believe that our reduced model is the appropriate framework to analyze the nonlinear corrections to the linear

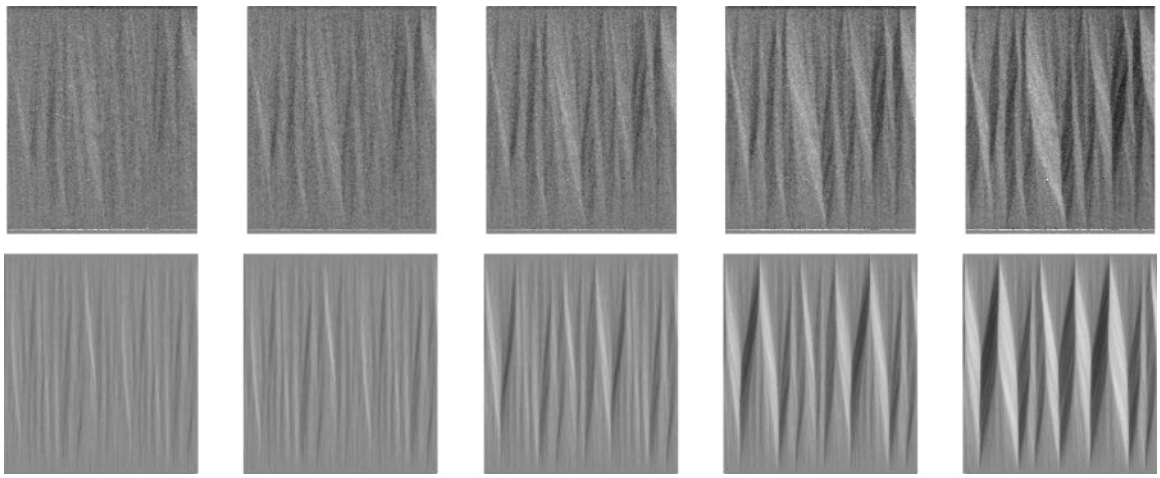

FIG. 33. Experiment and numerical simulations: The coarsening of the concertina pattern in a Permalloy sample (top row) of 30 nm thickness and 70 μm width compared to the numerical simulations (bottom row). A ripplelike structure grows into the concertina pattern. Within the numerical simulations we iteratively increment the external field and minimize the energy. The computational domain is of period $6\hat{w}^*$. The numerical images are scaled according to (12) to compare them to the experiment. The numerical images hence display 1.8 times the unit cell; the numerical images therefore appear to be more uniform than the experimental concertina.

ripple theory. Indeed, we have seen in Sec. II that it captures the transition from the unstable mode to low-angle symmetric Néel walls. We thus believe it also captures the transition from the ripple to the blocked state that is related to hysteresis in extended thin films.[26]

VI. UNIAXIAL ANISOTROPY

We now address the effect of uniaxial anisotropy—constant throughout the sample—on the formation of the concertina pattern. We focus on the two cases in which the easy axis coincides with the x_2 axis [transverse anisotropy $\mathbf{e} = (0,1,0)$ in Eq. (1)] or in which the easy axis coincides with the x_1 axis [longitudinal anisotropy $\mathbf{e} = (1,0,0)$ in Eq. (1)]. Clearly, the uniform magnetization remains a stationary point of the energy for this type of anisotropy. On the level of the reduced model both cases can be represented (up to an additive constant) by the additional quadratic term

$$-Q\,t\int m_2^2\,dx_1dx_2 \tag{38}$$

with a *signed* quality factor Q. Transverse anisotropy corresponds to $Q > 0$; longitudinal anisotropy corresponds to $Q < 0$.

As will become clear below, when considering the effects of anisotropy, it is appropriate to expand the Zeeman term to quartic order, i.e.,

$$-h_{\rm ext}t\int\left(m_2^2+\frac{m_2^4}{4}\right)dx_1dx_2.$$

The following gedanken experiment is helpful in understanding the sequel: In extended thin films, i.e., $\ell = \infty$, there is no incentive for a spatially varying magnetization so that we may consider a constant magnetization m_2 in which case the relevant energy per volume is given by $-Qm_2^2 - h_{\rm ext}(m_2^2 + \frac{m_2^4}{4})$. In this case the critical field is given by $h_{\rm ext}^* = -Q$. For longitudinal anisotropy, the bifurcation is subcritical, whereas for transverse anisotropy, the bifurcation is supercritical and yields

$$m_2 = \pm[2(1+Q^{-1}h_{\rm ext})]^{1/2}. \tag{39}$$

Hence, for finite ℓ, there are two competing mechanisms which lead to a bifurcation and the selection of an amplitude for m_2: uniaxial anisotropy and shape anisotropy in the form of the stray-field energy.

As we will see below, there are essentially three different effects of anisotropy: *linear*, *weakly nonlinear*, and *strongly nonlinear*, which we list and characterize below. Notice that the order at which these effects arise with increasing anisotropy does not agree with their ordering with increasing nonlinearity; see Fig. 34: The linear effect becomes pronounced for $|Q| \gg d^{2/3}\ell^{-4/3}t^{2/3}$, the strongly nonlinear one for $|Q| \gg \ell^{-1}t$, and the weakly nonlinear one only for $|Q| \gg d^{-2/3}\ell^{-2/3}t^{4/3}$. Note that we have that $d^{2/3}\ell^{-4/3}t^{2/3} \ll \ell^{-1}t \ll d^{-2/3}\ell^{-2/3}t^{4/3}$ provided $d^2\ell^{-1} \ll t$, which is the lower bound on the film thickness that characterizes regime III.

We mainly focus on the case of transverse anisotropy $Q > 0$. In the case of longitudinal anisotropy $Q < 0$ we give an explanation for the experimental fact that the concertina cannot be observed at all.

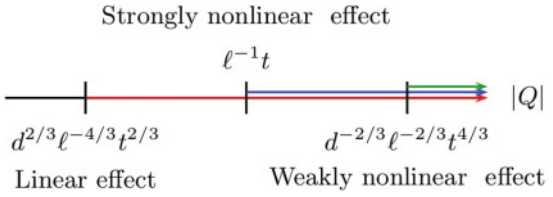

FIG. 34. (Color online) The order of the different effects of anisotropy.

(a) Linear effect for weak anisotropy $|Q| \gg d^{2/3}\ell^{-4/3}t^{2/3}$. An obvious effect of anisotropy is a shift of the critical field $h_{\rm ext}^*$ by the amount $-Q$; we call it the "linear effect" of anisotropy since it arises on the level of the linearization at $m_2 \equiv 0$. In view of the scaling of the critical field $h_{\rm ext}^*$ at $Q = 0$, i.e., (13), we infer that the value of the critical field is dominated by the uniaxial anisotropy, i.e.,

$$h_{\rm ext}^* \approx -Q \quad \text{for} \quad |Q| \gg d^{2/3}\ell^{-4/3}t^{2/3}. \tag{40}$$

Notice that transverse anisotropy decreases the distance between the two critical fields $\pm h_{\rm ext}^*$ corresponding to the stationary states $\pm\mathbf{m}^*$; in particular, for $Q \sim d^{2/3}\ell^{-4/3}t^{2/3}$, the critical field changes sign and thus the order between the two critical fields switches. (Likewise, for longitudinal anisotropy the distance decreases.) Although a clear-cut critical field cannot be observed in the experiments due to the polycrystalline structure which triggers a ripple, and since the value of the effective external field at the investigated sample section is not available, the linear effect could be qualitatively confirmed: For Permalloy samples of high (transverse) anisotropy the oscillatory instability occurs before the external field is reversed. In accordance with (40), we observe for relatively wide films that the relative strength of anisotropy increases and the critical field decreases (theoretically approaching $-Q$). On the other hand for low-anisotropic Permalloy the first oscillation is observed close to zero external field.

(b) Weakly nonlinear effect for strong anisotropy $|Q| \gg t(w^*)^{-1} \sim d^{-2/3}\ell^{-2/3}t^{4/3}$. For sufficiently strong anisotropy Q, the quartic term coming from the stray-field energy no longer dominates the quartic term coming from the Zeeman energy near the bifurcation. We call this effect the "weakly nonlinear effect" of anisotropy, since it can be analyzed on the level of an expansion of the reduced energy near $m_2 \equiv 0$ and $h_{\rm ext} = h_{\rm ext}^*$ [cf. (17)], where we take into account the quartic Zeeman term $-\frac{h_{\rm ext}}{4}tA^4\int(m_2^*)^4dx_1dx_2$. The shift of the critical field suggests the following rescaling for the reduced external field:

$$\hat{h}_{\rm ext} = d^{-2/3}\ell^{4/3}t^{-2/3}(h_{\rm ext}+Q).$$

In addition we set

$$\hat{Q} = -\tfrac{1}{4}d^{2/3}\ell^{2/3}t^{-4/3}h_{\rm ext}$$

so that we obtain with the same rescaling of energy, length, and magnetization as in Eqs. (12) and (14) the reduced energy

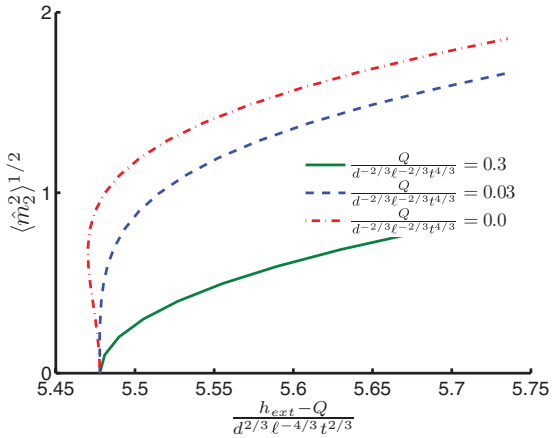

FIG. 35. (Color online) Numerical simulations: Transition from sub- to supercritical bifurcation as the strength of the transverse anisotropy increases. For $Q = 0.03 \approx Q^*$ the bifurcation degenerates.

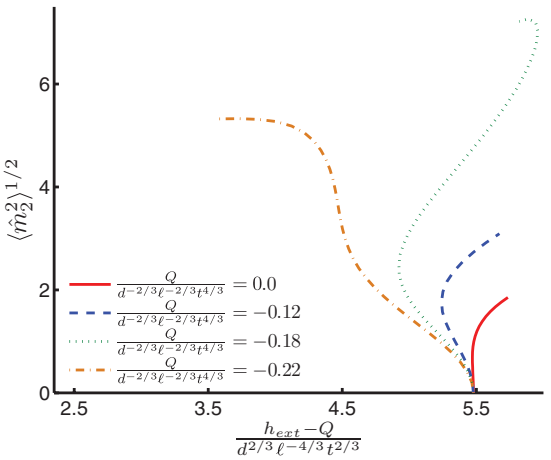

FIG. 36. (Color online) Numerical simulations: Loss of the turning point as the strength of the longitudinal anisotropy increases.

functional augmented by

$$+\hat{Q}\int_{\hat{\Omega}'} \hat{m}_2^4 d\hat{x}_1 d\hat{x}_2.$$

Therefore the energy close to the bifurcation takes the form of

$$\hat{E}(A\hat{m}_2^* + A^2\hat{m}_2^{**}) \approx -\left(\frac{\pi}{2}\right)^{1/3}(\hat{h}_{\text{ext}} - \hat{h}_{\text{ext}}^*)A^2 + \left(\frac{9}{64}\hat{Q} - \frac{\pi}{640}\right)A^4.$$

For $|Q| \gg d^{-2/3}\ell^{-2/3}t^{4/3} \gg d^{2/3}\ell^{-4/3}t^{2/3}$ the critical field asymptotically behaves as $h_{\text{ext}}^* \approx -Q$ [cf. (40)], so that the reduced quality factor behaves as $\hat{Q} \approx \frac{1}{4}d^{2/3}\ell^{2/3}t^{-4/3}\,Q$ close to the critical field. From the latter we read off that in the regime $Q \gg d^{-2/3}\ell^{-2/3}t^{4/3}$ the quartic coefficient becomes positive and therefore the bifurcation becomes supercritical; see Fig. 35. Essentially it is a perturbation of the constant-magnetization bifurcation in infinitely extended films mentioned above; cf. (39). In particular, the selected amplitude in this case scales as $m_2 \sim A \sim (1 + h_{\text{ext}}Q^{-1})^{1/2}$. On the level of the extended bifurcation analysis one finds that the period of the unstable mode w^* lies in the stable region in the neighborhood of the critical field. In agreement with this, for increasing external fields the numerical simulations show that no modulation instability occurs and that there is no coarsening. We note that domain theory is consistent with the numerical simulations, too.

On the other hand, for large longitudinal anisotropy, i.e., $-Q \gg d^{-2/3}\ell^{-2/3}t^{4/3}$, we expect that there is no turning point on the bifurcating branch so that it remains unstable, with the effect that no concertina pattern forms in the first place. The numerical simulations in Fig. 36 show a second turning point which coincides with the breakup of the concertina pattern. For even larger longitudinal anisotropy the first turning point is destroyed; see Fig. 36.

This observation can also be confirmed on the level of domain theory, where we take into account anisotropy and the quartic term in the Zeeman energy [cf. (25)]:

$$\begin{aligned} e_{\text{domain}}(m_2^0, w) = {} & 2\left(\ell - \frac{w}{m_2^0}\right)e(m_2^0) + 4\,\frac{w}{m_2^0}\,e\left(\frac{m_2^0}{2}\right) \\ & - (h_{\text{ext}} + Q)(m_2^0)^2 t\left(w\ell - \frac{w^2}{m_2^0}\right) \\ & - h_{\text{ext}}\frac{1}{4}(m_2^0)^4 t\left(w\ell - \frac{w^2}{m_2^0}\right). \end{aligned} \tag{41}$$

The quartic wall energy cannot compensate the destabilizing quartic Zeeman contribution provided $h_{\text{ext}}tw \gg t^2$ (up to a logarithm). Therefore because $h_{\text{ext}}^* \sim -Q$ and $w \sim d^{2/3}\ell^{2/3}t^{-1/3}$ close to the bifurcation there are no (local) minimizers of the energy.

Typical values for our Permalloy samples of strong uniaxial anisotropy range from $\hat{Q} = \frac{|Q|}{4d^{-2/3}\ell^{-2/3}t^{4/3}} \approx 2.1 \times 10^{-4}$ to 0.023 depending on the sample's width and thickness ($Q = 5 \times 10^{-4}$, $t = 10$–150 nm, $\ell = 10$–50 μm). Typical values for CoFeB range from $\hat{Q} = 7.8 \times 10^{-4}$ to 0.011 ($Q \approx 1.5 \times 10^{-3}$, $t = 30$–100 nm, $\ell = 10$–50 μm). The uniaxial anisotropy is thus too small to cause the weakly nonlinear effect. However, although local minimizers of the energy might exist in the case of longitudinal anisotropy, still the energy is not coercive as soon as the external field is reversed.

(c) Strongly nonlinear effects for moderate anisotropy $|Q| \gg \ell^{-1}t$. In that case one can distinguish two different scenarios in the formation of the concertina:

Scenario I. If the amplitude (and shape) of the concertina pattern were unaffected by anisotropy (except for the critical field at which it bifurcates), as in an infinitely extended film, its optimal amplitude would scale as

$$\begin{aligned} m_{2a} \sim \ell t^{-1}(h_{\text{ext}} - h_{\text{ext}}^*) &\overset{(40)}{\approx} \ell t^{-1}(h_{\text{ext}} + Q) \\ &= \ell t^{-1} Q(1 + Q^{-1}h_{\text{ext}}), \end{aligned} \tag{42}$$

up to a logarithm for $h_{\text{ext}} - h_{\text{ext}}^* \gg d^{2/3}\ell^{-4/3}t^{2/3}$, as we have seen in Eq. (27) in Sec. III A.

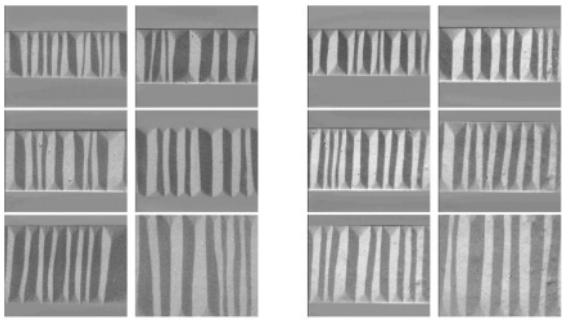

FIG. 37. Experiment: Permalloy samples of width 60–150 μm of high transverse anisotropy and at the end of the coarsening process. The *six* samples on the right are of thickness 30 nm, the six on the right of thickness 50 nm. The period of the pattern appears to be independent of the width of the samples, in agreement with our theoretical prediction as an effect of anisotropy.

Scenario II. If the amplitude of the concertina pattern were dominated by transverse anisotropy, it would behave as

$$m_{2a} \overset{(39)}{\sim} (1 + Q^{-1}h_{\text{ext}})^{1/2} \tag{43}$$

for $0 < (1 + Q^{-1}h_{\text{ext}}) \ll 1$.

Hence we expect that for $Q \gg \ell^{-1}t$ the concertina pattern is limited by stray-field effects as long as $0 < 1 + Q^{-1}h_{\text{ext}} \ll (Q^{-1}\ell^{-1}t)^2$ and by anisotropy effects once $(Q^{-1}\ell^{-1}t)^2 \ll 1 + Q^{-1}h_{\text{ext}} \ll 1$. Loosely speaking, the effect of anisotropy kicks in for a large amplitude and is most prominent close to the field strength where the concertina pattern vanishes. We call this the "strongly nonlinear effect" of anisotropy. (Also this provides a reason to expand the Zeeman term to higher order.)

We note that we have to take into account the lower-order wall energy in scenario II in order to determine the optimal period. In that case, a minimization of the energy per length yields the following scaling behavior of the optimal period (up to a logarithm):

$$w_a \sim (\ell t)^{1/2} Q^{-1/2} (1 + Q^{-1}h_{\text{ext}})^{1/4}.$$

As we know from Sec. III the experimentally more relevant quantity is the marginally stable period, i.e., the largest period (as a function of the external field) for which the minimal energy is convex. At the crossover we expect that the marginally stable period is of the order $\sim t\,Q^{-1}$, in accordance with the experimental observations; cf. Fig. 37. In fact, because $(Q^{-1}\ell^{-1}t)^2 \sim 1 + Q^{-1}h_{\text{ext}}$ at the crossover, we have that $w \sim \ell^2 t^{-1} Q(1 + Q^{-1}h_{\text{ext}}) \sim t\,Q^{-1}$; see (42) together with the fact that $w_s \sim \ell m_{2a}$. For a period of that order the minimal energy in scenario II turns out to be convex. Hence we expect that the coarsening stops once $(Q^{-1}\ell^{-1}t)^2 \ll 1 + Q^{-1}h_{\text{ext}} \ll 1$. Still the transverse component of the magnetization grows as $m_2 \sim (1 + Q^{-1}h_{\text{ext}})^{1/2}$ so that the size and height of the closure domains decrease.

Figure 38 displays the transition of the scaling behavior in the optimal period and the marginally stable period, and the amplitude of the transverse magnetization component. At the crossover we have that $m_2 \sim t(\ell Q)^{-1} \ll 1$ and $w \sim t\,Q^{-1} \ll \ell$. This is consistent with the assumptions of the reduced model, i.e., the low-angle approximation and the scale separation of the dominant length scales with respect to x_1 and x_2. For the same reason and due to the observation that $h_{\text{ext}} + Q \gg d^{2/3}\ell^{-4/3}t^{2/3}$ implies $\hat{h}_{\text{ext}} \gg 1$, (low-angle) domain theory is also applicable up to the crossover to scenario II. (As m_2 tends toward 1 in scenario II only domain theory is applicable and the low-angle approximation has to be dropped—in particular for the wall energy.)

Let us mention another observation supporting the conjecture that anisotropy effects are most prominent close to the field strength where the concertina vanishes: For $Q \gg \ell^{-1}t$, the ground state for vanishing external field $h_{\text{ext}} = 0$ is no longer given by the uniform magnetization $\mathbf{m} = (\pm 1,0,0)$; a Landau or concertina-type pattern (see Fig. 39), has lower

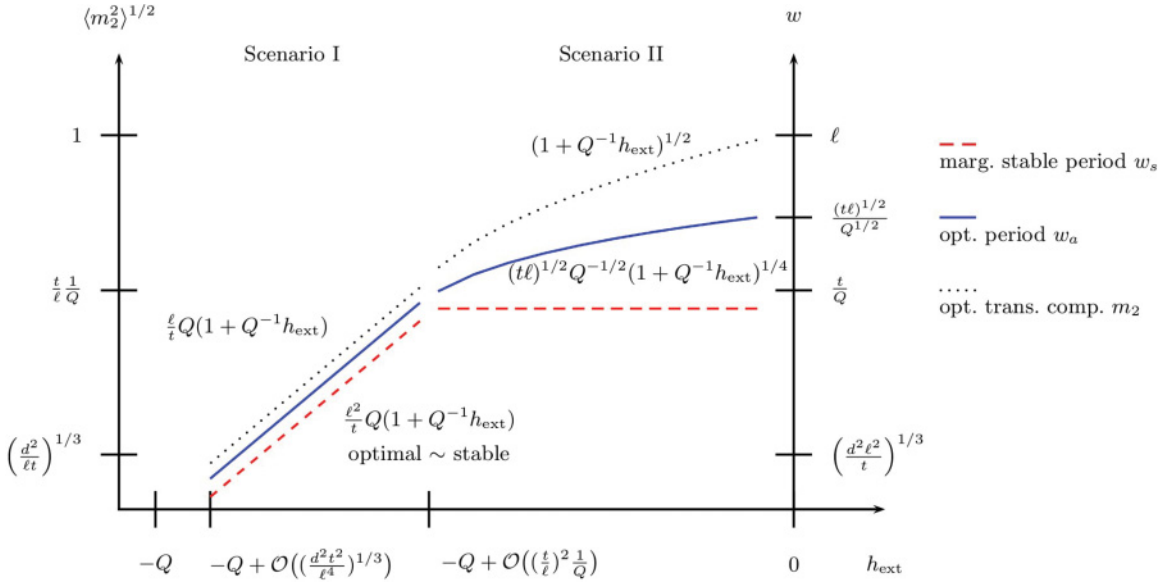

FIG. 38. (Color online) Scaling behavior of the optimal and marginally stable periods and the amplitude of the transverse component in the regime $t\ell^{-1} \ll Q \ll d^{-2/3}\ell^{-2/3}t^{4/3}$.

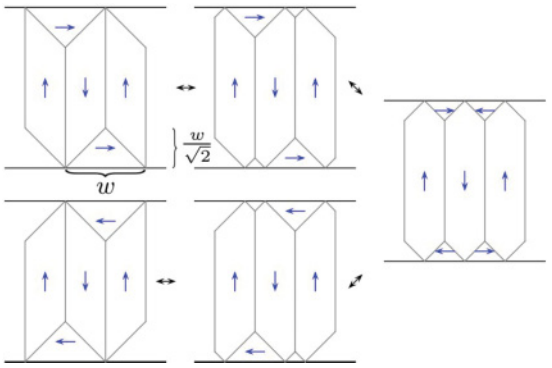

FIG. 39. (Color online) Continuous transition from the concertina pattern via the Landau state to the reversed concertina. Note that the total length of the walls and the Zeeman energy do not change while the anisotropy energy is smaller in the case of the Landau state.

energy. The optimal periods w of the two latter patterns are determined by a balance of the wall energy and the anisotropy energy in the closure domains, and scale as $w \sim Q^{-1/2}(\ell t)^{1/2}$ up to a logarithm. Hence we expect that in this regime, the concertina does not switch to $\mathbf{m} = (-1,0,0)$, but evolves to the pattern in Fig. 39.

In fact, that type of transition of the concertina pattern can be observed in CoFeB samples – that possess a stronger (transverse) uniaxial anisotropy; see Fig. 40.

VII. CONCLUSION

In this work, we addressed the concertina pattern in very elongated thin-film elements. We provided an explanation of the formation and the coarsening of this pattern as the external field is reduced from saturation.

We identified a parameter regime in which the uniform magnetization becomes unstable to an oscillatory buckling mode. In this parameter regime, we derived a two-dimensional and thus numerically tractable reduced energy functional from three-dimensional micromagnetics. On the basis of the reduced model, we performed numerical bifurcation analysis: The bifurcation is slightly subcritical, but has a turning point, after which the buckling mode grows into the concertina pattern with its low-angle Néel walls. This is an alternative explanation for the formation of the concertina to the one proposed by van den Berg and Vatvani: an outgrowth of an unstable mode instead of an ingrowth of closure domains. Over a wide range of sample sizes, there is a good agreement between the explicit period of the unstable mode and the measured average period of the concertina pattern. In particular, the predicted dependence on film thickness and width is confirmed. However, the measured period exceeds the theoretically predicted one by a factor of up to approximately 2.

We gave an argument for this initial deviation that at the same time explains the coarsening: Domain theory based on the reduced model—where low-angle Néel walls are replaced by sharp discontinuity lines—shows that coarsened configurations are energetically favorable. More importantly, uncoarsened configurations eventually become unstable because the energy per period becomes concave. Based on the reduced model, we argued by a Bloch-wave ansatz that this concavity indeed translates into a secondary instability of the concertina pattern with respect to long-wavelength modulations. These secondary instabilities are confirmed by numerical bifurcation analysis. The long-wavelength instabilities are further confirmed by an extended bifurcation analysis that capitalizes on the near degeneracy of the primary bifurcation. This extended bifurcation analysis also showed

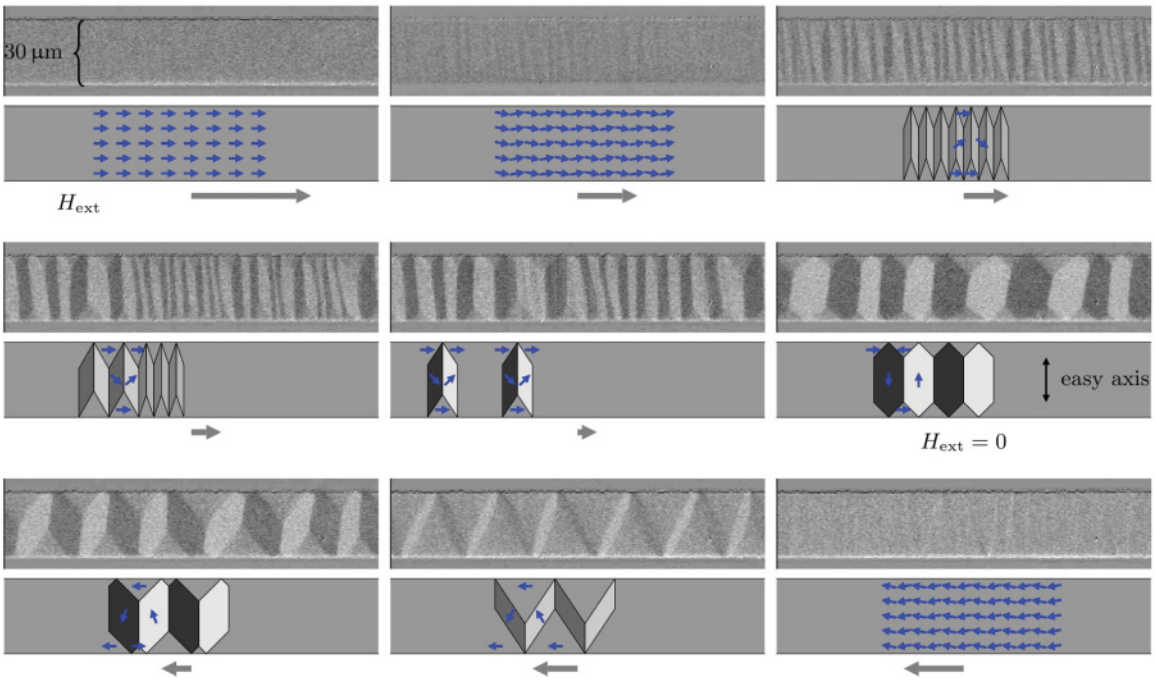

FIG. 40. (Color online) Experiment: Hysteresis of a CoFeB sample of 60 nm thickness and 30 μm width. Following the coarsening we observe a transition to a Landau state at zero external field, which turns into a concertina that degenerates and refines and finally disappears.

that the long-wavelength instability of the primary branch extends all the way down to the turning point. Hence, at the moment of its appearance, the concertina pattern already has a resulting period larger than that of the unstable mode. This qualitatively explains the deviation between the period of the unstable mode and the measured period of the concertina. Incidentally, these secondary instabilities are an asymmetric (with respect to the wave number) version of the Eckhaus instability introduced in the context of convective problems.

We gave yet another argument for the deviation of the period of the unstable mode from the measured period of the concertina at its formation. Based on the reduced model, we established a continuous transition from a magnetization ripple, which is triggered by the polycrystalline structure of the material, and the concertina pattern. On the level of the reduced model, the effect of an easy axis that varies from grain to grain translates into a random transverse external field that smears out the subcritical bifurcation. Hence for a sufficiently strong ripple effect, as the concertina pattern becomes discernible from the ripple, it has already coarsened.

Finally, we investigated the effects of weak uniaxial material anisotropy on the concertina pattern. We distinguished three effects: (1) a shift of the critical field that changes its sign already for weak anisotropies, (2) a change in the coarsened concertina pattern from "limited by shape anisotropy" to "limited by material anisotropy" that kicks in for somewhat larger anisotropies, and (3) a change from a subcritical to a supercritical bifurcation for a sufficiently large transverse anisotropy. The various analyses render a fairly complete picture of the energy landscape that in particular explains the hysteresis of the concertina pattern.

ACKNOWLEDGMENTS

J.M., R.S., and H.W. thank R. Mattheis and R. Kaltofen for help with the thin-film deposition. F.O. and J.S. thank Alexander Mielke for helpful discussions on the Eckhaus instability and Martin Zimmermann for technical support. Special thanks go to Ludwig Schultz (IFW) for supporting the Saxonian project "Teachers in Research," from which H.W. was funded, and for encouraging the collaboration between experimental and mathematical research on magnetic microstructures. The authors thank the unknown referees for their various suggestions that led to substantial improvement in the paper.

[1] H. van den Berg and D. Vatvani, IEEE Trans. Magn. **18**, 880 (1982).
[2] C. Kittel, Phys. Rev. **70**, 965 (1946).
[3] L. Landau and E. Lifshitz, Phys. Z. Sowjetunion **8**, 153 (1935).
[4] J. Jackson, *Classical Electrodynamics* (Wiley, New York, 1999).
[5] A. Hubert and R. Schäfer, *Magnetic Domains: The Analysis of Magnetic Microstructures* (Springer-Verlag, Berlin, 1998).
[6] A. Aharoni, *Introduction to the Theory of Ferromagnetism*, International Series of Monographs on Physics (Oxford University Press, Oxford, 2000).
[7] R. Cantero-Álvarez and F. Otto, J. Nonlinear Sci. **16**, 351 (2006).
[8] N. A. Usov, C.-R. Chang, and Z.-H. Wei, Phys. Rev. B **66**, 184431 (2002).
[9] P. Bryant and H. Suhl, Appl. Phys. Lett. **54**, 2224 (1989).
[10] A. DeSimone, R. V. Kohn, S. Müller, F. Otto, and R. Schäfer, Proc. R. Soc. London, Ser. A **457**, 2983 (2001).
[11] A. DeSimone, R. V. Kohn, S. Müller, and F. Otto, in *The Science of Hysteresis*, edited by G. Bertotti and I. Mayergoyz (Elsevier Academic Press, Amsterdam, 2005), Vol. 2, Chap. 4, pp. 269–381.
[12] R. Cantero-Álvarez and F. Otto, J. Nonlinear Sci. **16**, 385 (2006).
[13] K. Steenbeck and R. Mattheis, Phys. Rev. B **75**, 134419 (2007).
[14] K. Steenbeck, R. Mattheis, and M. Diegel, J. Magn. Magn. Mater. **279**, 317 (2004) .
[15] E. C. Stoner and E. P. Wohlfarth, Philos. Trans. R. Soc. London, Ser. A **240**, 599 (1948).
[16] R. Cantero-Álvarez, F. Otto, and J. Steiner, J. Nonlinear Sci. **17**, 221 (2007).
[17] J. Steiner, Diploma thesis, University of Bonn, 2006.
[18] C. Melcher, Arch. Ration. Mech. Anal. **168**, 83 (2003).
[19] F. Otto and J. Steiner, Calculus of Variations and Partial Differential Equations **39**, 139 (2010).
[20] W. Eckhaus, in *ICIAM 91, Washington, DC, 1991*, edited by R. E. O'Malley (SIAM, Philadelphia, 1992), pp. 83–98.
[21] J. Steiner, Doctoral thesis, University of Bonn, 2010.
[22] K. Georg, Numer. Funct. Anal. Optim. **22**, 303 (2001).
[23] M. Golubitsky and I. Stewart, *The Symmetry Perspective*, Progress in Mathematics, Vol. 200 (Birkhäuser-Verlag, Basel, 2002).
[24] H. Hoffmann, IEEE Trans. Magn. **4**, 32 (1968).
[25] K. J. Harte, J. Appl. Phys. **39**, 1503 (1968).
[26] E. Feldtkeller, Elektronische Rechenanlagen **3**, 167 (1961).